sustainability

MDPI

Article

Towards Sustainable Railways Using Polymeric Inclusions, Polyurethane Foam and Marginal Materials Derived from Rubber Tires

Piyush Punetha [1], Mohammad Adnan Farooq [1], Naveen Kumar Meena [2] and Sanjay Nimbalkar [1,*]

[1] School of Civil and Environmental Engineering, Faculty of Engineering and Information Technology, University of Technology Sydney, Ultimo, NSW 2007, Australia; piyush.punetha@uts.edu.au (P.P.); mohammadadnan.farooq@uts.edu.au (M.A.F.)
[2] Beca Pty. Ltd., Sydney, NSW 2000, Australia; naveen.meena@beca.com
* Correspondence: sanjay.nimbalkar@uts.edu.au

Abstract

Rail transport is widely regarded as a sustainable and environmentally friendly option for long-distance freight and passenger movement during its operation phase. However, its construction and maintenance phases often result in substantial environmental impacts, which must be addressed to improve the overall sustainability of railways. This study aims to identify solutions that improve the performance of railway tracks, reduce maintenance requirements, and minimize environmental impact. With this objective, the potential of artificial inclusions and innovative composite materials in enhancing the sustainability of railway tracks is investigated through a comprehensive methodology, combining experimental, analytical and numerical approaches. A novel composite material, comprising soil, scrap tire aggregates and an adhesive, demonstrated strong potential as a sustainable base layer for ballastless railway tracks, exhibiting minimal strain accumulation (0.29–0.98%) under 50,000 load cycles and adequate damping. Incorporation of cellular artificial inclusions in the substructure layers of ballasted tracks reduced cumulative settlement by up to 33% and slowed track geometry deterioration. Use of planar artificial inclusions beneath a pile-supported railway embankment enhanced the load transfer efficiency and curtailed settlement, while also lowering environmental impact by reducing concrete usage. The findings of this study highlight strong potential of these approaches in improving track performance and the overall sustainability of railways.

Keywords: composite; finite element; polymeric inclusions; railway tracks; rheological model; scrap rubber tires

Academic Editor: Grigorios L. Kyriakopoulos

Received: 6 September 2025
Revised: 3 October 2025
Accepted: 8 October 2025
Published: 11 October 2025

Citation: Punetha, P.; Farooq, M.A.; Meena, N.K.; Nimbalkar, S. Towards Sustainable Railways Using Polymeric Inclusions, Polyurethane Foam and Marginal Materials Derived from Rubber Tires. *Sustainability* **2025**, *17*, 9007. https://doi.org/10.3390/su17209007

1. Introduction

Rail transport is known for its sustainable attributes, such as emission of lower amounts of greenhouse gases and consumption of less energy than road or air transportation during its operation phase [1,2]. However, its construction and maintenance phases can have substantial environmental impacts [3]. These impacts primarily stem from the extraction, processing and transportation of tremendous quantities of virgin quarried material, use of cement, steel and heavy machinery as well as the generation of waste during construction and maintenance activities [4,5].

The carbon footprint of railway infrastructure is expected to rise due to two key factors: (a) the increasing frequency of maintenance and rehabilitation activities, driven by the

adoption of heavier axle load in freight trains and the operation of faster passenger trains; (b) the rapid expansion of railway networks, stimulated by urbanization. Addressing these challenges is crucial for enhancing the sustainability of railway transportation. Consequently, the railway industry is actively exploring effective strategies to strengthen track substructure and minimize the requirement for recurrent maintenance. Simultaneously, innovative approaches are being developed to lower the carbon footprint associated with the construction of new tracks, particularly on soils with poor engineering properties. These solutions should not only be cost-effective, but also have minimal impact on the environment, thereby contributing towards sustainable infrastructure development.

One promising approach involves the use of scrap tires in railway track construction and maintenance. With over 1.5 million tires being produced annually, their disposal remains a perplexing problem [6,7]. Repurposing them as construction materials in ballasted and ballastless railway tracks can mitigate both financial burdens and the environmental risks associated with their stockpiling or disposal in landfills. Past research has demonstrated that they can be used in various forms, such as whole tires [8], as mats fabricated from sidewalls or treads [9] or as aggregates [10,11].

Whole scrap tires have been employed in applications like retaining walls, erosion protection systems, breakwaters, and highway crash barriers [12,13]. Mats derived from sidewalls or treads have effectively been used to reinforce soil, leveraging their high tensile strength [9]. For instance, Yoon et al. [14] reported improved bearing capacity and reduced vertical settlement on reinforcing the soil using tire mats. Aggregates derived from scrap tires have potential applications as fill materials in embankments [15], backfill for retaining walls [16], drainage layers in highways [17] and vibration attenuation materials in railway tracks [18]. Past studies indicate that these aggregates show comparable performance to conventional materials in embankment and highway applications [19,20].

In the context of railway infrastructure, the incorporation of scrap tires in the form of granulated rubber improves the damping properties of track materials [7,21] and reduces particle breakage [22]. For example, Hidalgo-Signes et al. [18] reported a 95% increase in damping ratio when tire shreds (up to 10%) were mixed with granular soil. Wolfe et al. [23] found that the use of tire shreds beneath the ballast layer significantly reduced train-induced ground-borne vibrations. Guo et al. [24] observed that the crumb rubber-ballast mixture exhibits better force distribution compared to pure ballast, due to the cushioning effect provided by rubber particles. This also led to a reduction in the magnitude of contact forces, which can help in minimizing ballast breakage.

Despite these advantages, the addition of rubber aggregates to track materials can also result in reduced shear strength and increased settlement [25]. For instance, Gong et al. [22] found that the addition of aggregates derived from scrap tires (up to 10%) to ballast reduced its apparent cohesion and friction angle by 12.8% and 23.8%, respectively. Khoshoei et al. [26] reported that the vertical settlement increased with a rise in rubber content in rubber aggregate–steel slag ballast mixtures. To address these limitations, stabilizing agents such as polyurethane foam adhesive (PFA) can be employed. As discussed later in this article, the resulting soil–rubber–PFA composite exhibits improved damping properties and reduced plastic deformation. These properties are highly desired for application as a base layer in ballastless railway tracks.

Another sustainable approach is the utilization of artificial inclusions for strengthening the railway track substructure. These inclusions can be cellular, such as geocells, or planar, such as geotextiles, geogrids and geocomposites. Geocells are typically composed of polymer strips joined together at regular intervals, forming a three-dimensional (3D) cellular network that resembles a honeycomb. Similar to geocells, scrap tires can be

repurposed as cellular inclusions by connecting multiple units with metal clips, bars or ties [27].

The cellular inclusions typically reduce the horizontal movement of the infill soil under loading by providing lateral restraint and all-around confinement [28,29]. This property is advantageous for ballast and subballast layers of ballasted railway tracks, which are typically subjected to significant lateral deformation or spreading due to limited in-situ confinement. The installation of cellular inclusions in these layers can lead to reduced lateral movement and improved track performance [30].

It has been observed that reinforcing granular layers using cellular inclusions: (a) promotes uniform stress distribution over a wider subgrade area by increasing the stiffness of infill material [28,31]; (b) reduces or redistributes shear stresses at the interface between granular substructure layers and subgrade, depending on their installation location [32]; (c) enhances the strength and reduces permanent deformation of the infill material [30,33]. All these effects contribute to a slower rate of track geometry deterioration, thereby minimizing the need for frequent maintenance operations [34,35]. It must be noted that the performance of a reinforced granular layer depends on several factors such as the properties of inclusion, infill material and subgrade soil [36–38], position of inclusion within the track [39] and loading conditions [40]. A thorough evaluation of these factors is essential prior to their application within the railway track.

Previous field investigations have also demonstrated the effectiveness of cellular inclusions in railway applications. For instance, these inclusions have been shown to: (a) significantly reduce vertical settlement and lateral deformation in ballasted tracks [41]; (b) mitigate stiffness differences between the softer and stiffer sides of open track–bridge transitions, thereby enhancing their performance [35]. Despite their significant potential, the incorporation of cellular artificial inclusions in ballasted railway tracks remains elusive, primarily because of the absence of appropriate tools for assessing their effectiveness.

Planar inclusions can be used in pile-supported railway embankments (PSRE) constructed on soils with inferior engineering properties, such as high compressibility and low shear strength. The conventional pile-supported embankments typically require closely spaced piles to effectively transfer loads (self-weight and traffic-induced loads) to the subsoil [42]. However, closer spacing increases the number of piles, which could increase carbon emissions linked to the use of cement, steel and heavy machinery for their construction and installation. To enhance sustainability, planar inclusions such as geogrids, geocomposites or geotextiles can be employed [43–45]. These inclusions enhance the performance of PSRE through mobilization of tensioned membrane effect [46,47]. For instance, Liu et al. [42] reported that the incorporation of a planar inclusion significantly reduced differential settlement between piles and subsoil, as the inclusion carried a part of the load through tension generated within it. Several studies have investigated the role of planar inclusions in improving load-transfer mechanisms in PSRE. Their effectiveness in reducing subsoil settlement and improving load transfer to piles has been shown to depend on factors such as embankment height, pile spacing and pattern, subsoil properties, vehicle speed, inclusion stiffness and the number of inclusion layers [47–51]. However, most of these studies overlooked the effect of dynamic train loads on tensile stresses within the inclusions and the associated load-transfer mechanisms.

Despite technological advancements and escalating demands for high-speed and heavy-haul trains, research on effective sustainable approaches to enhance railway track performance under increased loading from these trains remains limited. In addition, there is a need to find sustainable alternatives to natural quarried aggregates for railway track construction and maintenance, due to significant environmental implications stemming

from their consumption. Particularly, the utilization of scrap tires and artificial inclusions as sustainable construction materials warrants further investigation.

This article assesses the performance of a novel composite material and two types of artificial inclusions through laboratory, analytical and numerical approaches. These materials have been identified as promising options to enhance the performance and sustainability of railway tracks based on a comprehensive review of alternatives. The article is structured as follows:

- Section 2 explores the effectiveness of a novel composite material, made from shredded scrap rubber tires, soil and PFA, as a sustainable base layer in ballastless railway tracks through laboratory investigations. In this composite, the granulated rubber contributes to damping while PFA provides strength and ductility.
- Section 3 investigates the adequacy of cellular artificial inclusions in strengthening railway tracks and minimizing the requirement for quarried materials using a computational approach that integrates a geotechnical rheological track model [52] with a confinement model for artificial inclusions [40].
- Section 4 examines the role of planar inclusions in reducing subsoil settlement and improving load transfer within a PSRE through finite element (FE) simulations. It also highlights the environmental benefits of using planar inclusions in PSRE.

2. Novel Composite Material for Ballastless Railway Tracks

2.1. General

The substructure of ballastless railway tracks typically comprises a concrete slab overlying cement–asphalt mortar, cement or lime-treated base, subbase and subgrade layers, as shown in Figure 1. While the cement-treated base layer provides adequate structural support, it contributes to the noise and vibration problem commonly associated with this type of track. In addition, although cement and lime enhance strength, they render the base layer brittle and susceptible to cracking. The use of cement also increases the carbon footprint of these tracks. Therefore, a composite material is proposed in this study for application in the base layer of ballastless railway tracks.

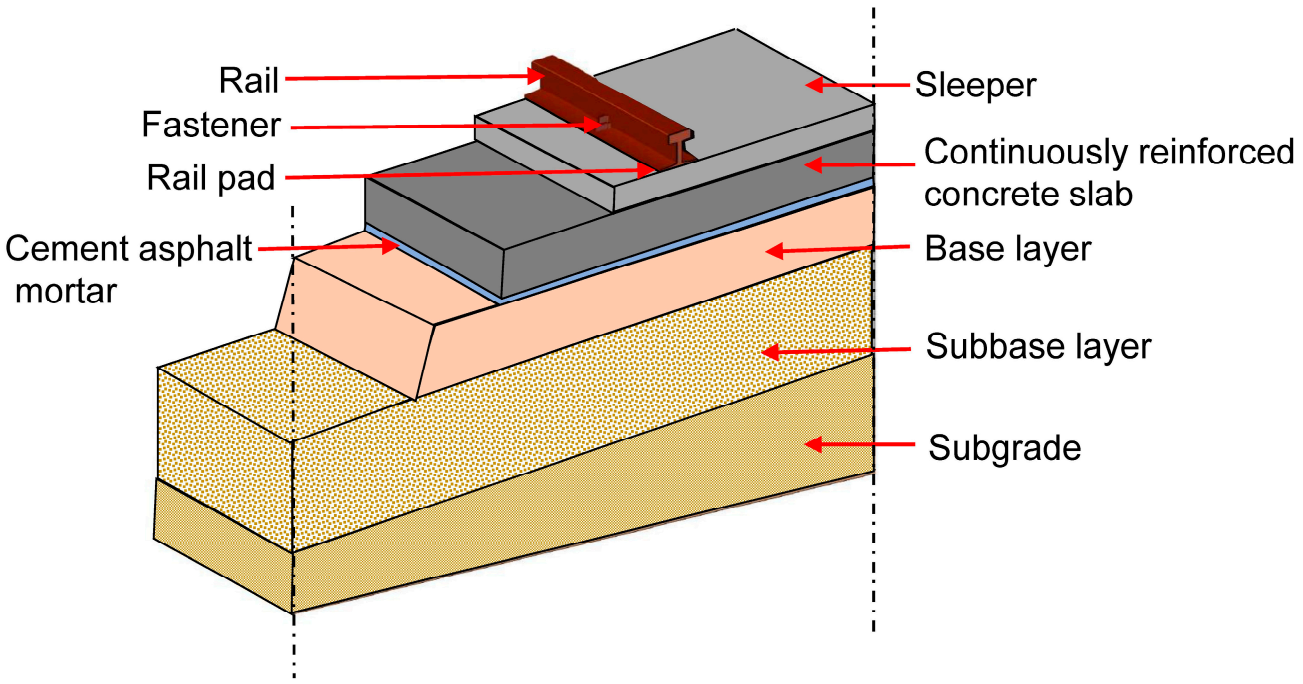

Figure 1. Schematic representation of a typical ballastless railway track.

2.2. Material Description

The composite proposed in the present study comprises three materials: soil (well-graded gravel), granulated rubber and PFA. All these materials were procured from local suppliers in Australia. Figure 2 depicts the grain size distribution (GSD) of the soil used in the present study. The terms "upper limit" and "lower limit" in the figure represent the acceptable range for GSD of base material according to the current industry standard [53]. It can be seen that the soil has a maximum particle size (d_{max}) of 19 mm and its gradation conforms to the current industry standard [53]. The mean particle size (d_{50}), uniformity coefficient (C_u) and coefficient of curvature (C_c) of the soil are 5.3 mm, 62.3 and 3.0, respectively. The specific gravity (G_s) of the soil is 2.73 (determined in accordance with AS 1289.3.5.1 [54]).

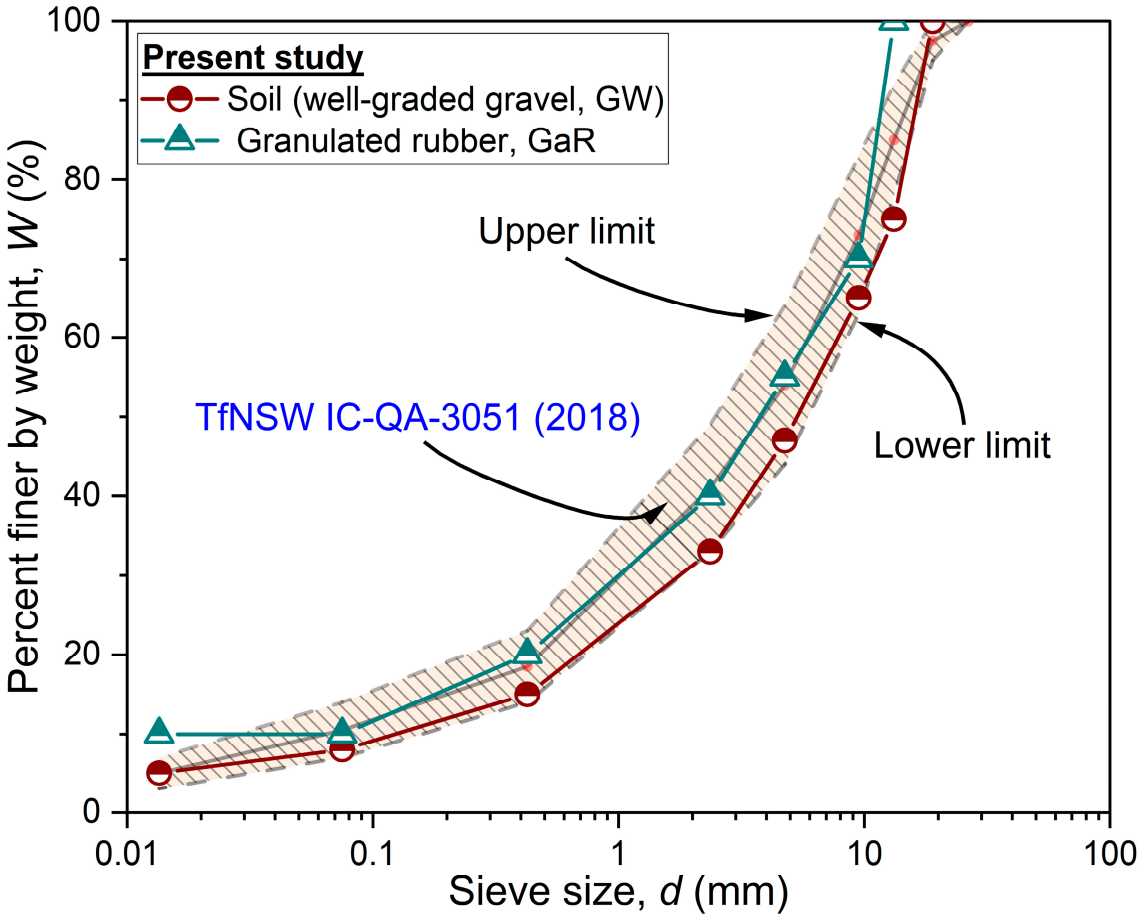

Figure 2. Grain size distribution curves of soil and granulated rubber used in the present study along with gradation limits for base material specified in TfNSW IC-QA-3051 [53].

The granulated rubber was derived from the end-of-life tires from trucks and passenger cars. These tires were first processed using a Tana Shark shredder, which reduced them into small-sized particles. These particles were further processed using another shredder, which removed all metal pieces. Nylon fibers were subsequently removed using a series of granulators. Finally, the scrap rubber was separated into different sizes [55]. In this study, rubber particles from six different size ranges between 0.075 mm and 13.2 mm have been used to achieve the target GSD shown in Figure 2. It has a d_{max}, d_{50}, C_u, C_c, and G_s of 13.2 mm, 3.8 mm, 75.0, 2.1, and 1.165, respectively.

A solvent-free, non-foaming, silicate-modified polyurethane resin, known as PFA, was used in this study. This non-foaming PFA was chosen for its ability to bind the soil and rubber particles without filling the voids, thus providing strength and ductility

to the composite mix while not significantly reducing permeability. It comprises two components: A and B (see Figure 3). Component A is transparent with a light straw color, while Component B is opaque with a dark brown color. The density of component A at 20° C ranges between 1300 and 1500 kg/m^3, whereas component B has a density ranging between 1150 and 1250 kg/m^3. Both components have a flash point greater than 200° C. The viscosity of components A and B varies from 120 to 350 mPa·s, and 50 to 300 mPa·s, respectively.

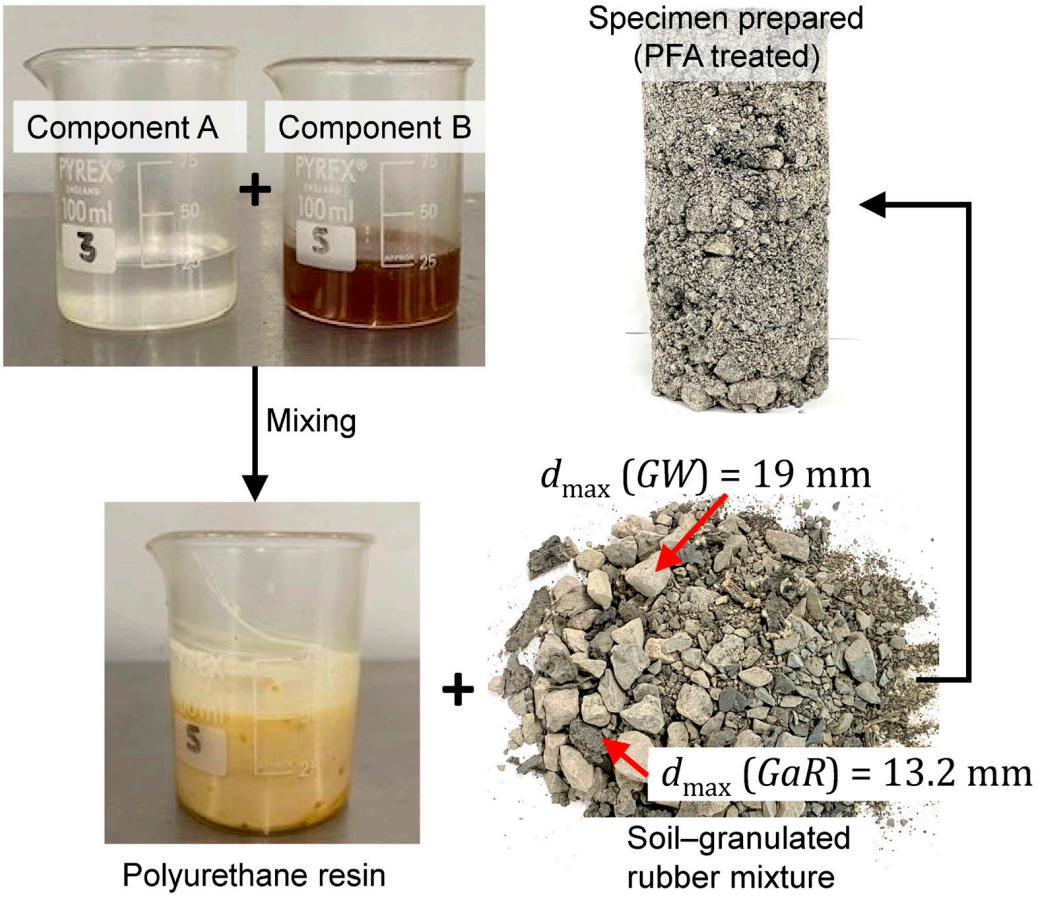

Figure 3. Preparation of soil–rubber–polyurethane foam adhesive (PFA) mixture samples (modified after [56]).

The sample preparation process of the soil–rubber–PFA mixture is shown in Figure 3. A 1:1 volume ratio (100:82 by weight) was used to combine components A and B at room temperature (25° C). Vigorous stirring for a few seconds initiated the chemical reaction between the two PFA components. After 30 s of agitation, the PFA was thoroughly mixed for two minutes with the soil–rubber mixture. The mixture was then compacted into five layers using the under-compaction technique to prepare a cylindrical specimen of diameter 100 mm and height 200 mm. More details on sample preparation can be found elsewhere [56,57].

It must be noted that the proportion of PFA and rubber granules in this study was fixed at 10% by mass of the mixture. This dosage was identified as optimal based on findings from static direct simple shear (SDSS) and cyclic direct simple shear (CDSS) tests [58]. In these tests, the percentage of rubber and PFA was varied between 0–25% and 0–20%, respectively. SDSS tests were used to evaluate the performance of mixtures under monotonic loading conditions in terms of cohesion, friction and dilation angles. CDSS tests were used to evaluate the long-term performance of mixtures under repeated loading for 50,000 load cycles under varying shear stress amplitude (50–200 kPa).

The optimum PFA dosage of 10% was based on achieving a significant improvement in strength, reflected by an increase in both cohesion and friction angles, with the most significant improvement occurring for PFA dosages of 7.5–12.5%. Beyond this, any further addition of PFA resulted in only marginal strength improvement. This dosage also triggered maximum dilative behavior, contributing to the highest shear strength, and most importantly, it substantially reduced the residual vertical strain under cyclic loading.

The residual vertical strain under cyclic loading remained low for rubber content of up to 15% but increased thereafter. In contrast, the damping ratio consistently increased with an increase in rubber content. An optimum rubber content of 10–20% was found to achieve desirable damping properties with the least negative impact on other characteristics, viz., cohesion, friction angle and shear modulus.

Thus, the optimum dosages of 10% PFA and 10% rubber adopted in this study were based on achieving a favorable balance of increased shear strength, minimized residual vertical strains, and enhanced damping. More details on the determination of optimum dosages of PFA and rubber are available in [58]. Furthermore, the obtained optimum dosage of rubber and PFA are in line with previous studies on scrap rubber, e.g., [7,59], which recommend optimum rubber dosage of 5–10%, and studies on PFA, e.g., [60,61], which recommend optimum PFA dosages of 5–15%.

2.3. Testing Procedure

Cyclic triaxial tests were performed to study the behavior of the soil–rubber–PFA composite under repeated loading conditions. The advanced triaxial testing equipment used in the present study is illustrated in Figure 4. Train loading was replicated by applying stress-controlled sinusoidal load cycles at a frequency (f) of 4 Hz. This frequency was determined based on the speed of trains and spacing between bogies, using the formula $f = V_t/(3.6\,\lambda)$, where V_t represents speed (km/h) and λ denotes spacing between bogies (m) [62,63]. The bogie spacing and train speed were considered 18 m and 260 km/h, respectively, which represents a cyclic frequency of 4 Hz.

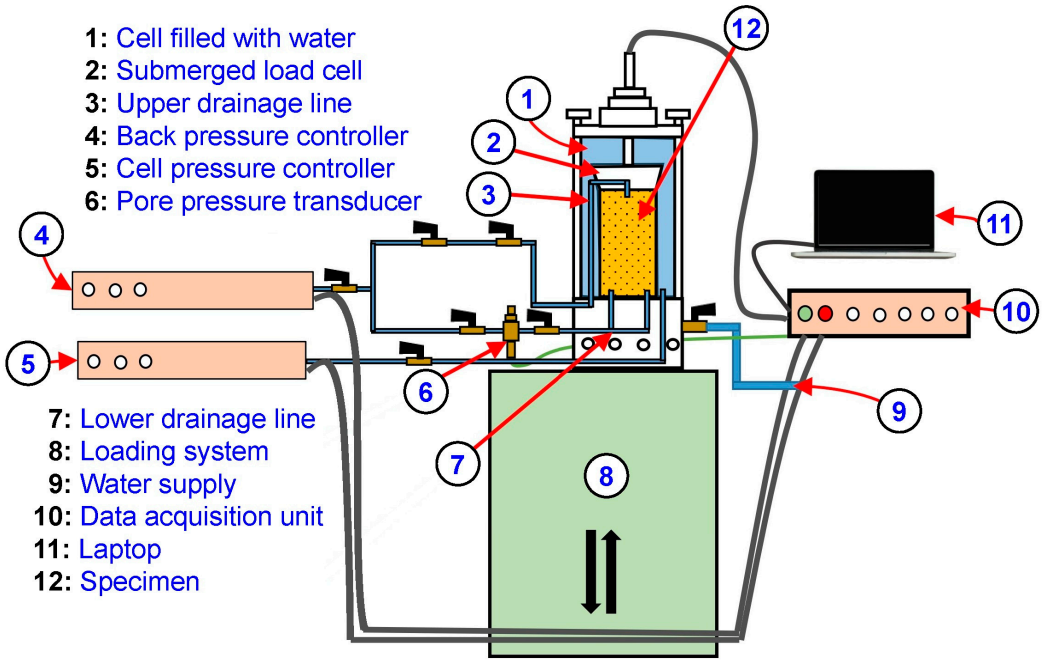

Figure 4. Schematic diagram of advanced triaxial testing equipment (modified after [64]).

A cyclic deviatoric stress amplitude (q_{cyc}) of 300 kPa was selected, which represents the stress level beneath the concrete slab of a ballastless track, as computed using FE

analyses [63]. An effective confining stress (σ'_3) of 10 and 50 kPa was selected to reflect conditions pertinent to ballastless railway tracks. Undrained loading conditions were chosen to replicate the high-speed track environment. The triaxial specimens were subjected to 50,000 load cycles (N) or until a vertical strain (ε_v) of 20% was reached, whichever occurred first.

In addition to the ternary mixture of soil, rubber and PFA, cyclic triaxial tests were conducted on binary mixtures, viz., soil–rubber, soil–PFA, and untreated soil for comparison purposes.

2.4. Results from Cyclic Triaxial Tests

2.4.1. Accumulation of Residual Vertical Strain

Figure 5 illustrates the accumulation of residual vertical strain (ε_{vr}) with the number of load cycles (N) for untreated soil and three mixtures at varying confinement levels (σ'_3 = 10 and 50 kPa). It can be observed that as σ'_3 increased, ε_{vr} decreased for all four samples. At σ'_3 = 10 kPa, the untreated soil failed after 260 cycles (ε_{vr}~20%), as shown in Figure 5a. When 10% rubber granules were added to the soil (without PFA treatment), ε_{vr} significantly increased, and the sample failed after N = 9. This abrupt failure can be attributed to reduced gravel particle interlock and the enhanced interparticle mobility provided by rubber particles. This increased ε_{vr} upon rubber incorporation under cyclic loading is consistent with previous studies [25,26,65–67]. When PFA was added to the untreated soil and the soil–rubber mixture, ε_{vr} decreased significantly, and both these samples withstood 50,000 cycles. Soil–PFA and soil–rubber–PFA mixtures exhibited ε_{vr} of 0.17% and 0.98%, respectively, at the end of test. All samples, except the soil–rubber mixture, withstood 50,000 cycles at higher confinement, i.e., σ'_3 = 50 kPa (Figure 5b). The soil–rubber–PFA mixture exhibited ε_{vr} of 0.29% after 50,000 cycles at σ'_3 = 50 kPa. These results indicate that the composite material will not undergo excessive deformation under train-induced repeated loading.

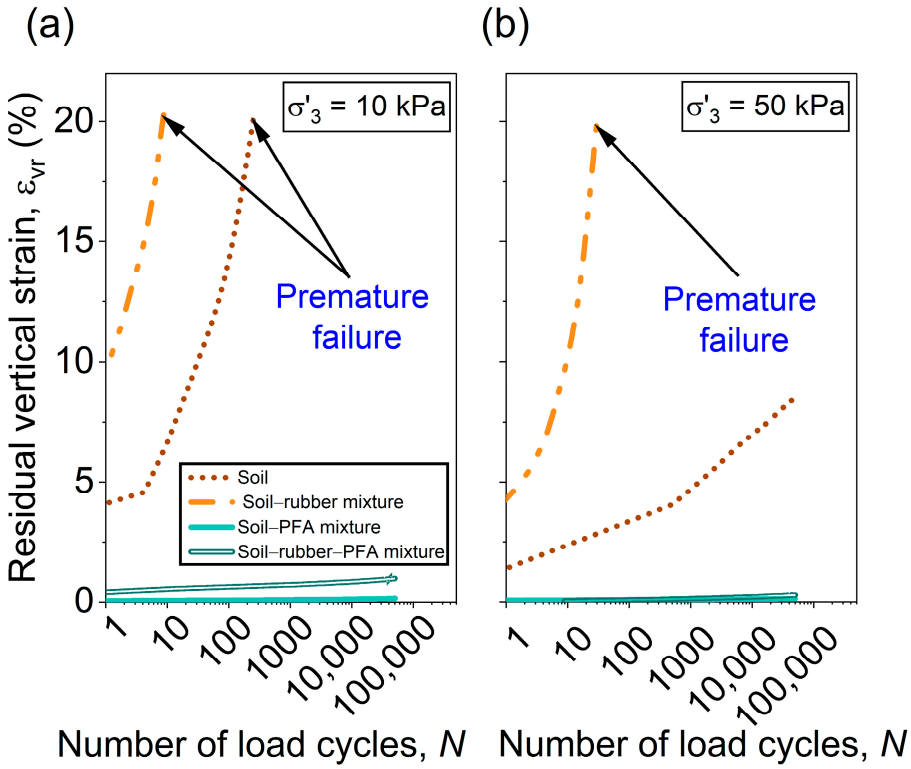

Figure 5. Accumulation of residual vertical strain with increasing number of load cycles at an effective confining stress of (**a**) 10 kPa; (**b**) 50 kPa.

2.4.2. Pore Water Pressure Variations

Figure 6 illustrates the variation of change in pore water pressure (Δu) with N at σ'_3 = 10 and 50 kPa. It is apparent that at σ'_3 = 10 kPa, Δu remains negligible ($\leq$10 kPa) for soil–PFA and soil–rubber–PFA mixtures. The untreated soil exhibits negative Δu during the initial stages, which decreases with an increase in N. However, for the soil–rubber mixture, Δu becomes more negative with an increase in N.

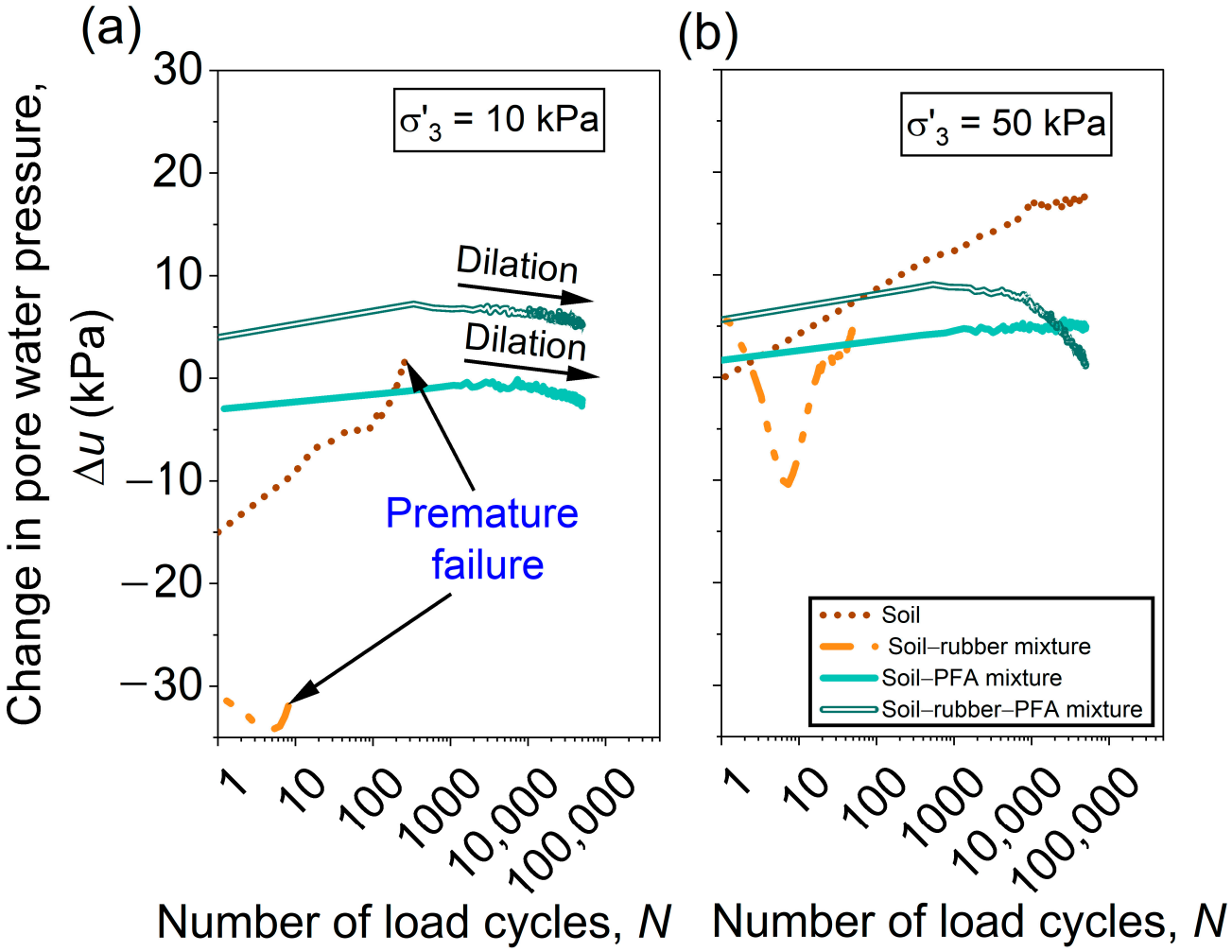

Figure 6. Variation of change in pore water pressure with increasing number of load cycles at an effective confining stress of (**a**) 10 kPa; (**b**) 50 kPa.

Under low confinement, the rubber particles might prevent the soil particles from rearranging into a denser packing. This creates temporary voids, which result in the observed negative pore water pressure. This negative Δu then reduces as the rigid soil particles gradually migrate into the spaces created by the deformed rubber. A similar pattern was reported by Madhusudhan et al. [68] for a rubber–sand mixture.

At σ'_3 = 50 kPa, untreated soil shows a sharp rise in Δu within the first 1000 cycles, while Δu for the soil–rubber–PFA mixture increased gradually. A drop in Δu for this mixture after N = 4000 suggests dilation due to PFA cementation. The soil–PFA mixture exhibits minimal Δu, whereas Δu for the soil–rubber–PFA mixture reached $\approx$5 kPa and 1 kPa at σ'_3 = 10 and 50 kPa, respectively, after N = 50,000.

These results highlight that PFA reduces cumulative deformation and excess pore water pressure buildup; thus, its application in the base layer will improve the performance of track substructure irrespective of the confinement levels.

2.4.3. Shear Modulus and Damping Ratio Variations

Evaluation of shear modulus (G) and damping ratio (D_R) of track materials is essential to understand their behavior under train-induced dynamic loading. The G values are computed using Equation (1) [69].

$$G = \frac{E}{2(1+\nu)} \quad (1)$$

where E is the elastic modulus calculated using the slope of the line passing through the extreme points of the hysteresis loop, as shown in Figure 7; ν is Poisson's ratio (considered 0.5 for the undrained specimen). It must be noted that G computed in the present study is the secant shear modulus (G_{sec}) but is referred to as shear modulus for simplicity.

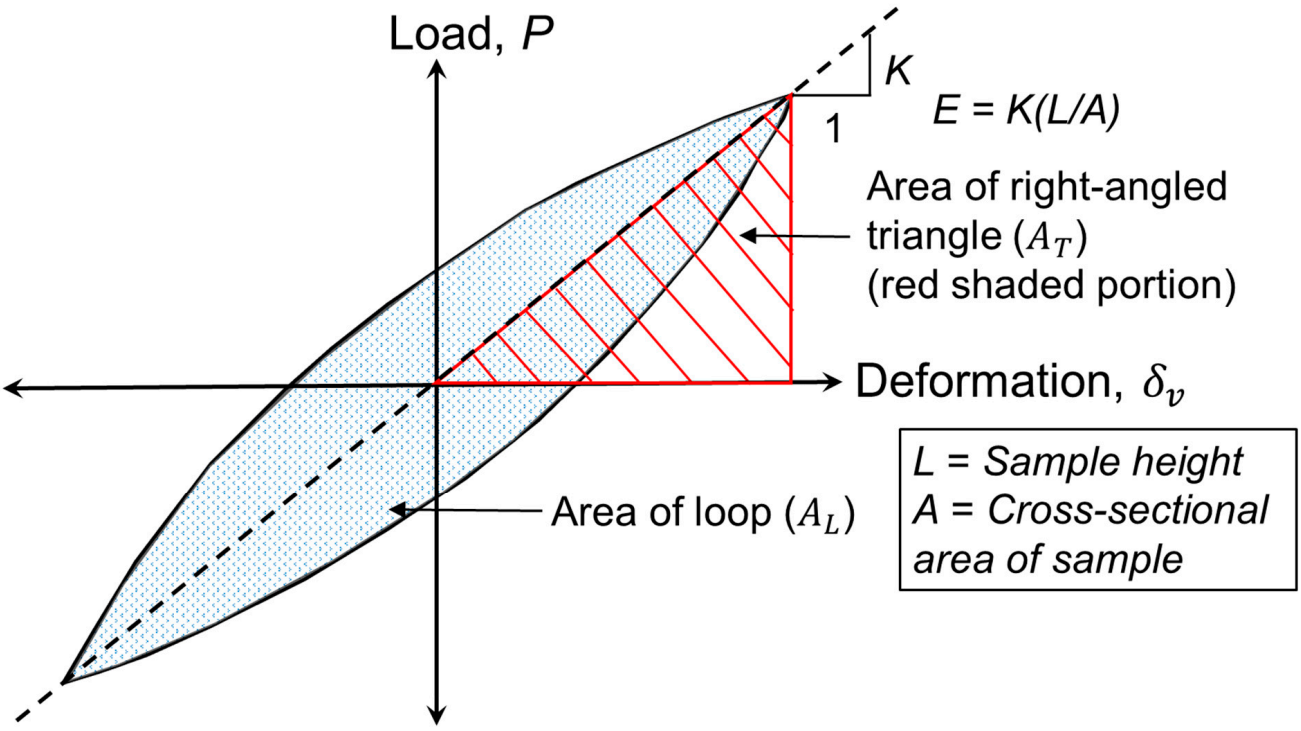

Figure 7. Determination of shear modulus and damping ratio (modified after [58]).

The D_R is calculated using the area of the hysteresis loop and the right-angled triangle (representing the maximum energy stored during a load cycle) (see Figure 7). This D_R represents the capacity of a soil to dissipate energy for each loading cycle [70] and can be computed using Equation (2).

$$D_R = \frac{A_L}{4\pi A_T} \quad (2)$$

where A_L and A_T = areas enclosed by the hysteresis loop and the right-angled triangle (refer to Figure 7), respectively.

Figure 8 illustrates the variation in G and D_R with N for untreated soil and the three mixtures under σ'_3 of 10 and 50 kPa. It is apparent that the incorporation of rubber to untreated soil increases D_R but reduces G. Conversely, G increases upon adding PFA to untreated soil while D_R decreases. The confining pressure also influences both G and D_R, with higher σ'_3 leading to increased G and reduced D_R.

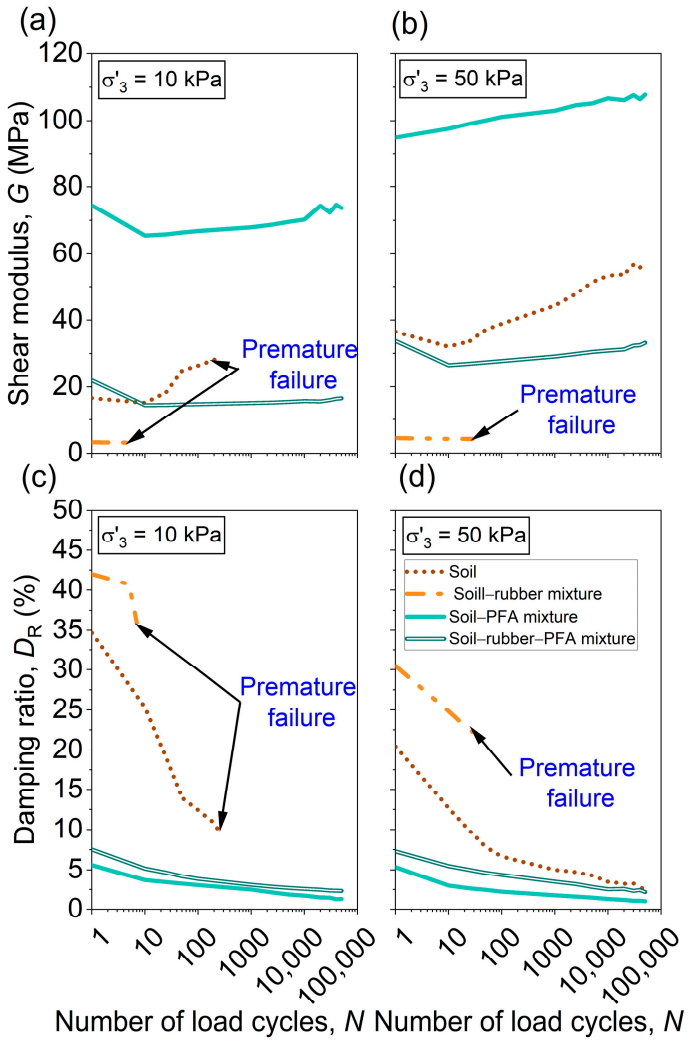

Figure 8. Variation in shear modulus with increasing number of load cycles at an effective confining stress of (**a**) 10 kPa; (**b**) 50 kPa; Variation in damping ratio with increasing number of load cycles at an effective confining stress of (**c**) 10 kPa; (**d**) 50 kPa.

To quantify the individual effects of adding rubber and PFA on the behavior of different mixtures, their dynamic properties (G and D_R) are compared at the 10th loading cycle under σ'_3 = 10 kPa. This comparison reveals that the addition of rubber to soil primarily enhances its energy dissipation capacity, with 61% increase in D_R at 10% rubber content compared to untreated soil. However, this improvement in damping is accompanied by a substantial reduction in stiffness (a 79% decrease in G). In contrast, PFA acts as a stabilizing agent that significantly increases the stiffness of the mixture, with a 333% increment in G value at 10% PFA content compared to untreated soil. However, this stiffness improvement is accompanied by a significant reduction in energy dissipation capacity, as indicated by an 85% decrease in D_R.

Interestingly, the ternary mixture (soil–rubber–PFA) demonstrates a balanced performance. Compared to the soil–PFA mixture, this mix achieved a 39.4% improvement in D_R with a 78% decrease in G value. Despite the reduction in G, the mixture showed superior long-term stability and withstood 50,000 cycles with minimal deformation (ε_{vr} = 0.98%), thereby outperforming the binary mixtures (soil–rubber and soil–PFA).

2.4.4. Permeability

The coefficient of vertical permeability (k_v) for different mixtures was also determined at the end of the consolidation stage before cyclic loading. After completion of the consolidation stage, a significant reduction in k_v was observed for untreated soil and soil–rubber mixture. This reduction in k_v was due to a decrease in the void ratio of the sample, which occurs during consolidation. The reduction in k_v increased with an increase in σ'_3. Insignificant changes in k_v were observed for the soil–PFA and soil–rubber–PFA mixtures. Also, σ'_3 did not influence k_v of these PFA-treated mixtures. Thus, using these treated mixtures in the base layer of ballastless railway tracks would avoid the build-up of excess pore pressure by offering an uninterrupted water flow under varying confinement levels.

The k_v values for different mixtures after consolidation under various σ'_3, are illustrated in Figure 9. It can be observed that the k_v of soil is 5.7×10^{-5} m/s after consolidation under σ'_3 of 10 kPa, and it decreases to 4.7×10^{-5} m/s with the addition of 10% rubber. Madhusudhan et al. [71] and Masad et al. [72] also noted a decrease in k_v with the addition of rubber to soil. Soil–PFA and soil–rubber–PFA mixtures exhibit k_v of 5.8×10^{-5} m/s and 5.9×10^{-5} m/s, respectively, which are similar to untreated soil. PFA was added to the soil–rubber mixture to bind the soil and rubber particles together. This prevented the particles from moving during the saturation stage and made it easier for water to flow. Therefore, the soil–rubber–PFA mixture did not show a decrease in k_v. Notably, non-foaming PFA was utilized in the present study at an ideal dosage that was adequate to cover the particles without filling in the gaps, which could have decreased the permeability.

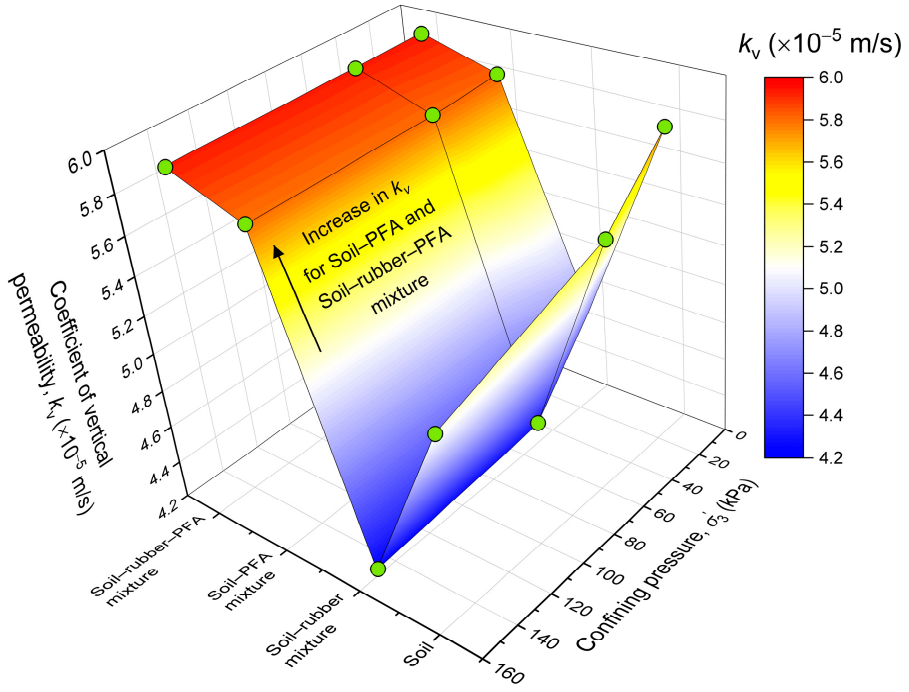

Figure 9. Permeability of different mixtures under varying confining pressure.

2.5. Limitations and Future Scope

A direct comparison of the performance of the novel composite with cement-treated soil was beyond the scope of this study due to the limitations of the testing equipment. Such a comparison would have enabled a more comprehensive evaluation of the performance of the composite, and it will be addressed in future research. This study also did not explore the micro-level interactions between soil, rubber particles and PFA within the proposed composite material. Understanding these interactions is essential for gaining

deeper insights into the long-term performance of this material under varying mechanical and environmental loading conditions. Future investigations shall address this limitation by conducting microstructural analysis using techniques such as scanning electron microscopy. In addition, advanced modeling approaches, such as the discrete element (DE) method, would be employed to simulate particle-scale interactions and accurately predict the mechanical behavior of this material.

2.6. Concluding Remarks

This section assessed the effectiveness of a novel composite material, comprising soil, aggregates derived from discarded tires, and PFA, in enhancing the performance and sustainability of the railway tracks through laboratory investigations. The main findings from this section are as follows:

- The novel composite material demonstrates strong potential as a sustainable base layer for ballastless railway tracks. This composite exhibited negligible cumulative residual vertical strain (0.29–0.98%) and minimal residual pore water pressure (~1–10 kPa) after 50,000 load cycles.
- The composite showed superior damping performance for vibration attenuation and a high permeability, reflecting improved drainage.

These findings highlight that the proposed soil–rubber–PFA composite offers a sustainable alternative for the base layer in ballastless railway tracks. This novel composite contributes to sustainability by:

- Promoting utilization of a significant industrial waste stream through repurposing of granulated rubber from end-of-life tires, thereby alleviating landfill burden.
- Substituting carbon-intensive cement with a polyurethane-based resin (i.e., PFA), which significantly reduces the embodied carbon and overall greenhouse gas emissions linked to the construction of track substructure.

These environmental benefits are achieved while ensuring the novel composite meets the engineering performance criteria for ballastless railway tracks. Thus, the composite presents an effective solution that integrates high performance with environmental stewardship. It must be noted that a quantitative assessment of the reduction in carbon footprint achieved using the novel composite is beyond the scope of this study and is a subject of future research.

3. Using Cellular Artificial Inclusions in Railway Tracks

3.1. General

The granular substructure layers of ballasted railway tracks (e.g., ballast and subballast) typically experience low inherent confinement and limited lateral restraint. This insufficient confinement often leads to lateral movement under repetitive train loading, resulting in track geometry degradation [73]. Over the past few decades, increased axle loads and traffic volume have exacerbated this degradation [74]. Consequently, frequent maintenance operations have become necessary to restore track geometry to acceptable levels, contributing to the increased carbon footprint of the railway infrastructure.

The issue of inadequate confinement and lateral restraint can be mitigated by reinforcing the substructure layers with 3D cellular artificial inclusions, such as geocells or discarded rubber tires. Several field studies have also demonstrated the benefits of incorporating these inclusions in track substructure layers [34,35,41]. However, despite significant potential, their use in railway tracks is still limited due to a lack of appropriate methods for evaluating their effectiveness.

Researchers have employed various numerical methods to assess the adequacy of these inclusions on the long-term performance of railway tracks [75–79]. However, these approaches, particularly DE and FE methods, demand significant computational resources and entail considerable time for reliable evaluation of the track response, especially under several load cycles. Analytical methods are relatively faster and computationally more efficient options to DE or FE methods for predicting the performance of reinforced ballasted railway tracks. However, these methods remain relatively underexplored. The following section utilizes a computational methodology developed by Punetha and Nimbalkar [30] to evaluate the adequacy of cellular artificial inclusions in strengthening the ballasted railway tracks.

This approach integrates a geotechnical rheological model for ballasted tracks [52] with a confinement model for artificial inclusions [40]. The confinement model estimates the additional confining pressure exerted by the inclusions on the infill soil. This additional pressure is incorporated into the rheological framework to evaluate the response of reinforced ballasted tracks subjected to repeated train loading.

3.2. Ballasted Railway Track Model

Figure 10 depicts the geotechnical rheological model of a ballasted track. This model consists of several mass elements interconnected by springs, dashpots (or dampers) and slider elements to simulate the mechanical behavior of the track substructure. Three substructure layers are modelled: ballast, subballast (also referred to as permeable capping) and subgrade. The cellular artificial inclusion is assumed to be installed at the bottom portion of the ballast layer. Train wheels are idealized as moving point loads travelling in the longitudinal ($+x$) direction along the track (see Figure 10). The spacing between the wheels is considered identical to that of an Acela Express passenger train. The vertical component of the rail seat load exerted on the substructure layers is computed using the beam-on-elastic-foundation method [80].

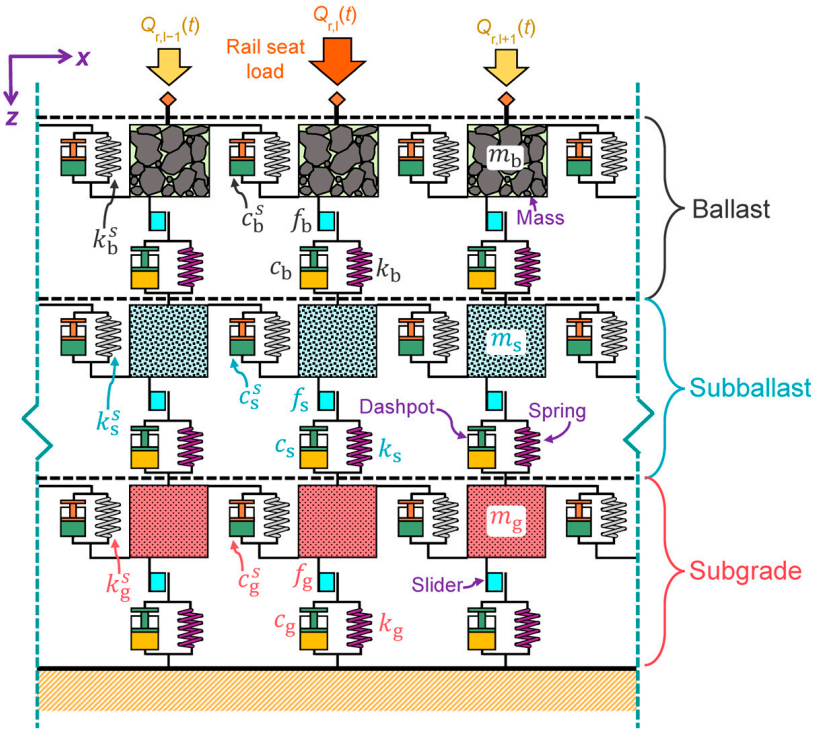

Figure 10. A ballasted railway track model (modified after [64]).

In this methodology, three stages of track response are predicted. The first stage represents initial loading, when a train wheel moves towards the target location (e.g., below the *l*th sleeper), and the stress state in the substructure layers is within their yield surfaces defined by f_b, f_g and f_s for ballast, subgrade and subballast, respectively. In this stage, viscoelastic elements (springs and dashpots) are activated; however, the plastic elements (sliders) remain deactivated, resulting in a viscoelastic track response. In the second stage, the stress state in the substructure layers satisfies their yield criteria [81] and loading conditions [82], thereby activating the sliders and resulting in a viscoelastic-plastic response. The movement of plastic elements is irreversible, and its magnitude is governed by their constitutive relations, which are detailed in Punetha and Nimbalkar [81]. The third stage represents unloading, i.e., when the train wheel moves away from the target location. During this phase, viscoelastic elements deform while the plastic elements remain inactive and retain their positions (which were attained after the completion of the second stage). These stages are repeated with the arrival of the next wheel.

The total response of the track substructure layers is computed by solving the following equation of motion at every time instant [30]:

$$\begin{aligned} \boldsymbol{M}d\ddot{\boldsymbol{v}}_{\mathbf{l}} + \boldsymbol{C}d\dot{\boldsymbol{v}}_{\mathbf{l}} + \boldsymbol{K}d\boldsymbol{v}_{\mathbf{l}} - \boldsymbol{C}^{\mathbf{p}}d\dot{\boldsymbol{v}}^{\mathbf{p}}_{\mathbf{l}} - \boldsymbol{K}^{\mathbf{p}}d\boldsymbol{v}^{\mathbf{p}}_{\mathbf{l}} - \boldsymbol{C}^{\mathbf{s}}\left\{d\dot{\boldsymbol{v}}_{\mathbf{l}-1} + d\dot{\boldsymbol{v}}_{\mathbf{l}+1}\right\} - \boldsymbol{K}^{\mathbf{s}}\left\{d\boldsymbol{v}_{\mathbf{l}-1} + d\boldsymbol{v}_{\mathbf{l}+1}\right\} + \boldsymbol{C}^{\mathbf{p},\mathbf{s}}\left\{d\dot{\boldsymbol{v}}^{\mathbf{p}}_{\mathbf{l}-1} + d\dot{\boldsymbol{v}}^{\mathbf{p}}_{\mathbf{l}+1}\right\} \\ + \boldsymbol{K}^{\mathbf{p},\mathbf{s}}\left\{d\boldsymbol{v}^{\mathbf{p}}_{\mathbf{l}-1} + d\boldsymbol{v}^{\mathbf{p}}_{\mathbf{l}+1}\right\} = d\boldsymbol{Q} \end{aligned} \tag{3}$$

where

$$\boldsymbol{M} = \begin{bmatrix} m_g & 0 & 0 \\ 0 & m_s & 0 \\ 0 & 0 & m_b \end{bmatrix}; \boldsymbol{C} = \begin{bmatrix} 2c_g^s + c_g + c_s & -c_s & 0 \\ -c_s & 2c_s^s + c_s + c_b & -c_b \\ 0 & -c_b & 2c_b^s + c_b \end{bmatrix}; \boldsymbol{K} = \begin{bmatrix} 2k_g^s + k_g + k_s & -k_s & 0 \\ -k_s & 2k_s^s + k_s + k_b & -k_b \\ 0 & -k_b & 2k_b^s + k_b \end{bmatrix} \tag{4}$$

$$\boldsymbol{C}^{\mathbf{p}} = \begin{bmatrix} 2c_g^s + c_g & -c_s & 0 \\ 2c_s^s & 2c_s^s + c_s & -c_b \\ 2c_b^s & 2c_b^s & 2c_b^s + c_b \end{bmatrix}; \boldsymbol{K}^{\mathbf{p}} = \begin{bmatrix} 2k_g^s + k_g & -k_s & 0 \\ 2k_s^s & 2k_s^s + k_s & -k_b \\ 2k_b^s & 2k_b^s & 2k_b^s + k_b \end{bmatrix}; \boldsymbol{C}^{\mathbf{s}} = \begin{bmatrix} c_g^s & 0 & 0 \\ 0 & c_s^s & 0 \\ 0 & 0 & c_b^s \end{bmatrix}; \boldsymbol{K}^{\mathbf{s}} = \begin{bmatrix} k_g^s & 0 & 0 \\ 0 & k_s^s & 0 \\ 0 & 0 & k_b^s \end{bmatrix} \tag{5}$$

$$\boldsymbol{C}^{\mathbf{p},\mathbf{s}} = \begin{bmatrix} c_g^s & 0 & 0 \\ c_s^s & c_s^s & 0 \\ c_b^s & c_b^s & c_b^s \end{bmatrix}; \boldsymbol{K}^{\mathbf{p},\mathbf{s}} = \begin{bmatrix} k_g^s & 0 & 0 \\ k_s^s & k_s^s & 0 \\ k_b^s & k_b^s & k_b^s \end{bmatrix}; d\boldsymbol{Q} = \begin{Bmatrix} 0 \\ 0 \\ dQ_{r,l} \end{Bmatrix}; d\ddot{\boldsymbol{v}}_{\mathbf{l}} = \begin{Bmatrix} d\ddot{v}_{g,l} \\ d\ddot{v}_{s,l} \\ d\ddot{v}_{b,l} \end{Bmatrix}; d\dot{\boldsymbol{v}}_{\mathbf{l}} = \begin{Bmatrix} d\dot{v}_{g,l} \\ d\dot{v}_{s,l} \\ d\dot{v}_{b,l} \end{Bmatrix}; d\boldsymbol{v}_{\mathbf{l}} = \begin{Bmatrix} dv_{g,l} \\ dv_{s,l} \\ dv_{b,l} \end{Bmatrix} \tag{6}$$

$$d\dot{\boldsymbol{v}}^{\mathbf{p}}_{\mathbf{l}} = \begin{Bmatrix} d\dot{v}^{p}_{g,l} \\ d\dot{v}^{p}_{s,l} \\ d\dot{v}^{p}_{b,l} \end{Bmatrix}; d\boldsymbol{v}^{\mathbf{p}}_{\mathbf{l}} = \begin{Bmatrix} dv^{p}_{g,l} \\ dv^{p}_{s,l} \\ dv^{p}_{b,l} \end{Bmatrix}; d\dot{\boldsymbol{v}}_{\mathbf{l}-1} = \begin{Bmatrix} d\dot{v}_{g,l-1} \\ d\dot{v}_{s,l-1} \\ d\dot{v}_{b,l-1} \end{Bmatrix}; d\dot{\boldsymbol{v}}_{\mathbf{l}+1} = \begin{Bmatrix} d\dot{v}_{g,l+1} \\ d\dot{v}_{s,l+1} \\ d\dot{v}_{b,l+1} \end{Bmatrix}; d\boldsymbol{v}_{\mathbf{l}-1} = \begin{Bmatrix} dv_{g,l-1} \\ dv_{s,l-1} \\ dv_{b,l-1} \end{Bmatrix} \tag{7}$$

$$d\boldsymbol{v}_{\mathbf{l}+1} = \begin{Bmatrix} dv_{g,l+1} \\ dv_{s,l+1} \\ dv_{b,l+1} \end{Bmatrix}; d\dot{\boldsymbol{v}}^{\mathbf{p}}_{\mathbf{l}-1} = \begin{Bmatrix} d\dot{v}^{p}_{g,l-1} \\ d\dot{v}^{p}_{s,l-1} \\ d\dot{v}^{p}_{b,l-1} \end{Bmatrix}; d\dot{\boldsymbol{v}}^{\mathbf{p}}_{\mathbf{l}+1} = \begin{Bmatrix} d\dot{v}^{p}_{g,l+1} \\ d\dot{v}^{p}_{s,l+1} \\ d\dot{v}^{p}_{b,l+1} \end{Bmatrix}; d\boldsymbol{v}^{\mathbf{p}}_{\mathbf{l}-1} = \begin{Bmatrix} dv^{p}_{g,l-1} \\ dv^{p}_{s,l-1} \\ dv^{p}_{b,l-1} \end{Bmatrix}; d\boldsymbol{v}^{\mathbf{p}}_{\mathbf{l}+1} = \begin{Bmatrix} dv^{p}_{g,l+1} \\ dv^{p}_{s,l+1} \\ dv^{p}_{b,l+1} \end{Bmatrix} \tag{8}$$

where dv, $d\dot{v}$ and $d\ddot{v}$ = displacement, velocity and acceleration increments, respectively; c = damping coefficient; k = stiffness; m = mass of a substructure layer; dQ_r = increment in the vertical component of rail seat load. The subscripts g, s, and b denote subgrade, subballast and ballast, respectively; subscripts l, $l-1$ and $l+1$ represent the lth, previous and next to lth sleeper, respectively; superscripts p and s represent the plastic and shear components, respectively. $\boldsymbol{M}$, $\boldsymbol{C}$ and $\boldsymbol{K}$ = mass, damping and stiffness matrices, respectively; $d\boldsymbol{v}$, $d\dot{\boldsymbol{v}}$ and $d\ddot{\boldsymbol{v}}$ = displacement, velocity and acceleration increment vectors, respectively; $d\boldsymbol{Q}$ is the rail seat load increment vector. The m, c and k values of the substructure layers are evaluated using a method detailed in [83,84]. This method requires the values of resilient modulus, Poisson's ratio, thickness and density of track substructure layers.

3.3. Evaluation of Additional Confinement

The cellular artificial inclusion restrains the movement of the infill material and provides additional confinement in the longitudinal and transverse directions (x and y). This extra confinement can be calculated as follows [40]:

$$\Delta\sigma_x = -\frac{2M_i}{D_i}\left[\frac{(1-\nu_i)k_i+\nu_i}{(1+\nu_i)(1-2\nu_i)}\right]\varepsilon_x \quad (9)$$

$$\Delta\sigma_y = -\frac{2M_i}{D_i}\left[\frac{(1-\nu_i)k_i+\nu_i}{(1+\nu_i)(1-2\nu_i)}\right]\varepsilon_y \quad (10)$$

where $\Delta\sigma_x$ and ε_x = additional confining stress and strain in infill along x direction, respectively; $\Delta\sigma_y$ and ε_y = additional confining stress and strain in infill along y direction, respectively; k_i, M_i, ν_i, and D_i = circumferential to radial strain ratio, mobilized modulus, Poisson's ratio and equivalent diameter of the cellular inclusion, respectively.

3.4. Prediction of Track Response

The behavior of a reinforced ballasted track subjected to repeated train loading is predicted through the following procedure:

1. Compute the m, c and k values of the substructure layers (refer to [83]).
2. Evaluate the vertical component of rail seat load at all sleeper locations for individual time steps. Determine stress distribution within track substructure using the modified Boussinesq approach (refer to [52]).
3. At every time step, check if the yield and loading/unloading conditions of plastic sliders are satisfied. If so, calculate the inelastic deformations (refer to [81]).
4. Compute the additional confining stress provided by the inclusions in both longitudinal (x) and transverse (y) directions (Equations (9) and (10)).
5. Calculate the total displacement of substructure layers by solving Equation (3) using Newmark's numerical integration approach.
6. Update the stress state based on the computed additional confining stress.
7. Repeat steps 3 to 6 for the desired number of wheel passages to obtain the complete displacement time history.

All these calculations have been carried out in this study using a MATLAB (version 2021a) code [85].

3.5. Validation

The accuracy of the proposed computational approach in simulating the behavior of reinforced ballasted railway tracks is assessed by comparing its predictions with results from 3D FE analyses conducted by Satyal et al. [39]. In their study, Satyal et al. [39] developed FE models for ballasted railway tracks, both with and without cellular artificial inclusions. These models were previously validated against experimental plate loading tests performed on both unreinforced and cellular inclusion-reinforced ballast overlying weak subgrade soil [39]. Figure 11 illustrates a comparison of the settlement predicted using the proposed approach with that from FE analyses conducted by Satyal et al. [39]. The material parameters used in the validation are provided in Table 1 and Appendix A. It is apparent from the figure that the settlement values computed using the proposed approach are in good agreement with those predicted from FE analyses (typically 3–8% variation in results). The proposed approach can accurately predict the decrease in track settlement resulting from the installation of cellular inclusion at the bottom portion of ballast layer (for both ballast layer thicknesses).

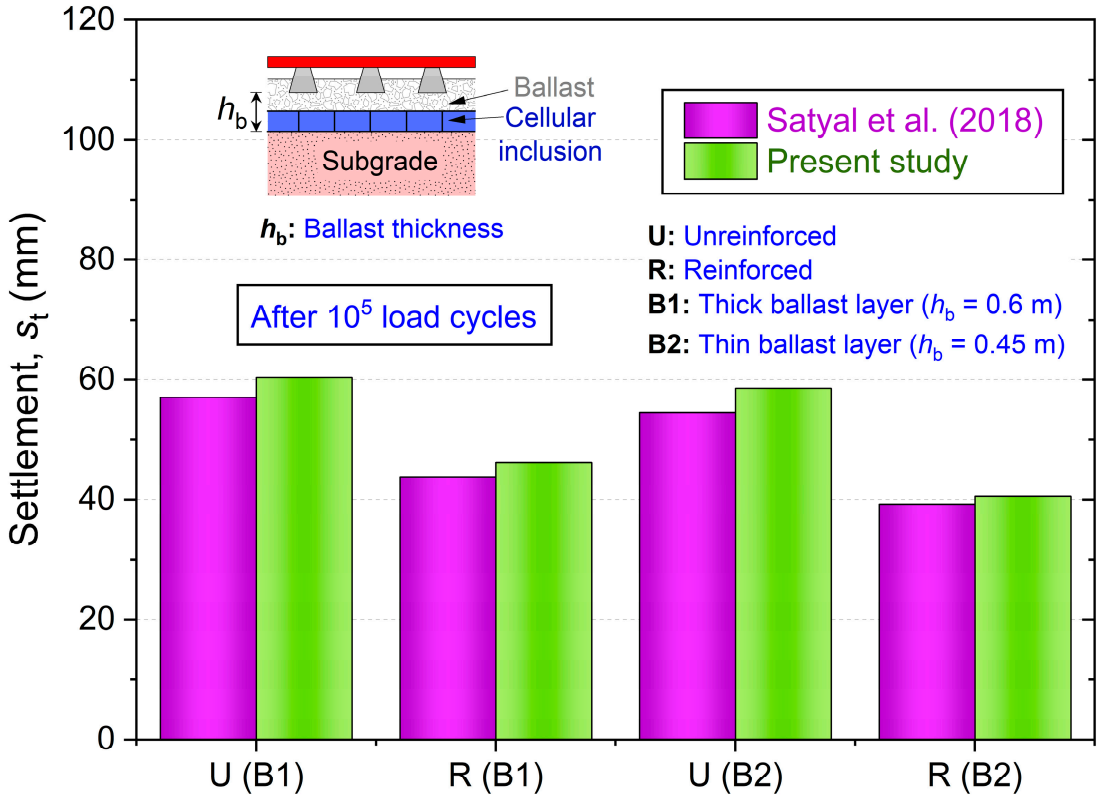

Figure 11. Comparison of track settlement computed using proposed approach with results from finite element (FE) analysis reported by Satyal et al. [39].

Table 1. Material parameters used in validation (data sourced from [30,39]).

Parameter	Ballast	Subgrade	Inclusion
Thickness/height, h (m)	0.45–0.6	2	0.15
Density, ρ (kg/m^3)	1500	2162	950
Resilient modulus, M_r (MN/m^2)	30	8.5	-
Poisson's ratio, ν	0.4	0.35	0.35
Diameter, D (m)	-	-	0.3

3.6. Results and Discussion

The proposed computational methodology has been used to assess the effectiveness of cellular artificial inclusions in (a) curtailing cumulative settlement in railway tracks; (b) mitigating environmental impacts by reducing the demand for natural aggregates. The effect of inclusion properties, such as material type, installation location and wheel load on the performance of reinforced track is investigated. Table 2 lists the values of parameters considered in the simulations, which have been selected based on the published literature. It must be noted that the resilient modulus (M_r) of subgrade is within the typical range of M_r values for weak subgrade reported in the literature (i.e., between 7–28 MPa) [73,86]. The constitutive parameters for plastic sliders are provided in Appendix A. The nominal case considers a high-density polyethylene (HDPE) inclusion, installed at the bottom of the ballast layer. M_i of the inclusion is the secant modulus corresponding to mobilized strain, which is determined from the load versus strain curves derived from tension tests (see Figure 12).

Table 2. Material parameters used in simulations (data sourced from [30]).

Parameter	Ballast	Subballast	Subgrade	Inclusion
Thickness/height, h (m)	0.3	0.15	6	0.15
Density, ρ (kg/m^3)	1760	1920	1920	935
Resilient modulus, M_r (MN/m^2)	200	115	20	-
Poisson's ratio, ν	0.3	0.4	0.45	0.3
Diameter, D (m)	-	-	-	0.25

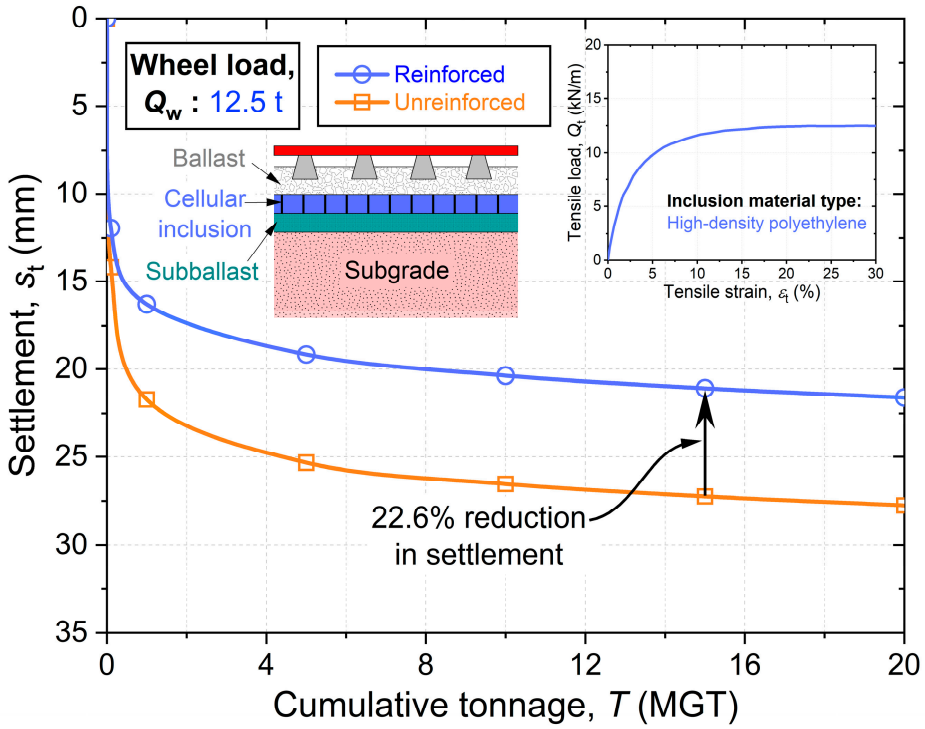

Figure 12. Track settlement plotted versus tonnage for reinforced and unreinforced ballasted track.

3.6.1. Response Comparison of Unreinforced and Reinforced Track

Figure 12 illustrates the accumulation of settlement with tonnage for reinforced and unreinforced ballasted railway tracks. It is apparent that the track settlement decreases upon reinforcing the ballast bottom with cellular HDPE inclusions. After a cumulative tonnage of 15 million gross metric tons (MGT), the incorporation of inclusions reduced the track settlement by 22.6% in comparison to the unreinforced case. Thus, the use of cellular artificial inclusions leads to a slower rate of track geometry degradation.

The influence of wheel load, installation location and material type on the settlement reduction is explored in the next sections.

3.6.2. Influence of Wheel Load

The wheel load can significantly affect the long-term performance of reinforced railway tracks. Therefore, its effect is studied by varying wheel load from 10 to 15 t. Figure 13 depicts the effect of wheel load on the performance of unreinforced and reinforced ballasted tracks. It is apparent that the wheel load increment leads to a rise in track settlement for both unreinforced and reinforced tracks. For the unreinforced track, the settlement accumulated over a tonnage of 15 MGT rises by 41.6% on increasing the wheel load from 10 to 15 t. This increment is due to a rise in stresses within the track substructure with increasing wheel load. For the reinforced case, the settlement also increases with a rise in wheel

load, albeit with a smaller magnitude. For example, after 15 MGT, the settlement rises by 38.2% on increasing the wheel load from 10 to 15 t. However, the magnitude of settlement accumulated after 15 MGT for reinforced track at 15 t wheel load is 23.3% smaller than the unreinforced case. This indicates that inclusions maintain their effectiveness even at higher wheel loads.

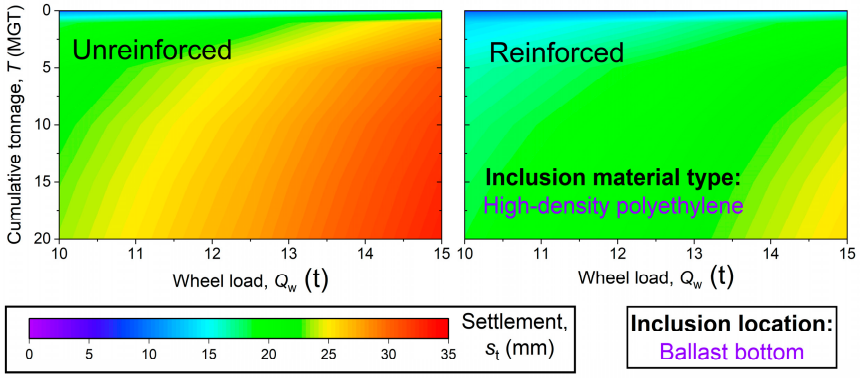

Figure 13. Influence of wheel load on settlement for unreinforced and reinforced track.

3.6.3. Influence of Installation Location

The location of the inclusion within the track substructure could also influence its performance. To identify the most effective placement location, the performance of inclusions installed at the bottom of the ballast, subballast and top of the subgrade is assessed. Figure 14 illustrates the influence of inclusion location on track settlement when subjected to a cumulative tonnage of 15 MGT. It is apparent that the inclusions provide maximum reduction in settlement (22.6%) when they are used at the bottom of the ballast layer. This observation is plausible, as there is limited inherent confinement in the ballast layer for the unreinforced case. The cellular inclusion provides additional confinement and lateral restraint, which decreases the deformation considerably, leading to a reduction in track settlement. Thus, the effectiveness of artificial inclusions can be enhanced by placing them strategically within the railway track.

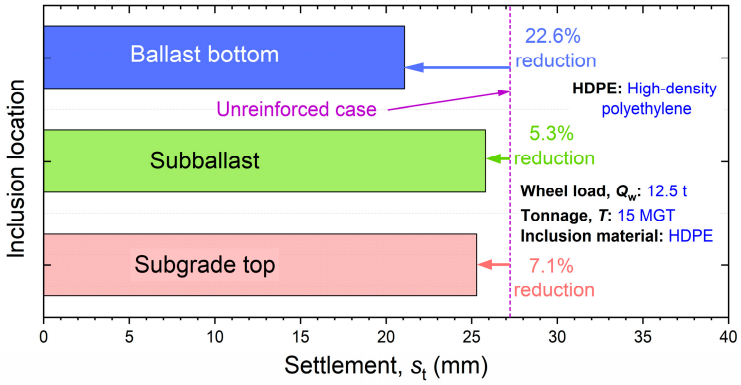

Figure 14. Track settlement when inclusions are installed at different locations.

3.6.4. Effect on Granular Layer Thickness Requirements

Generally, the thickness of granular layers is increased to minimize the stress transmitted to the subgrade layer and consequently, reduce the settlement, especially when the subgrade is weak. By installing cellular artificial inclusions in the subgrade top, it could be possible to curtail the required thickness of granular substructure layers without affecting track performance. This is highlighted in Figure 15, which compares the subgrade settlement when the thickness of the subballast layer is increased from 0.15 to 0.2 m

and when inclusions are provided at the subgrade top. It is evident that the reduction in subgrade settlement is similar for both cases. Thus, subballast thickness can be reduced by 25% by reinforcing the subgrade top with artificial inclusions, thereby lowering overall costs and minimizing environmental impact. This approach is particularly beneficial when high-quality subballast material is not locally available, which would otherwise lead to substantial economic and environmental consequences associated with the extraction, processing, and transportation of quarried subballast material.

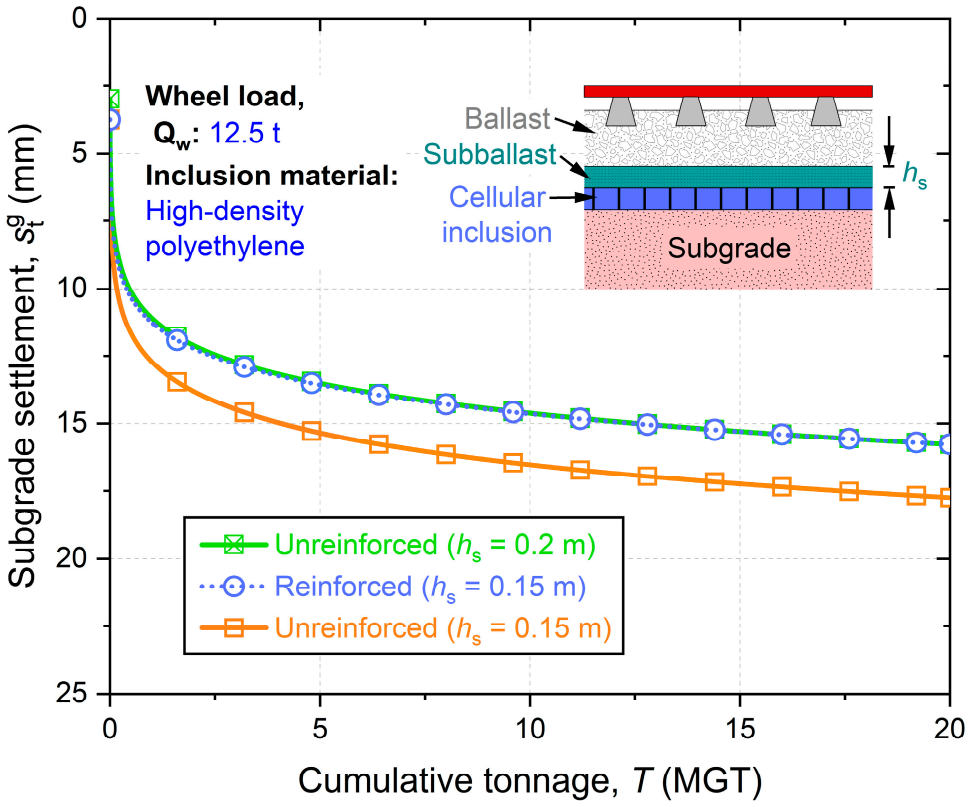

Figure 15. Accumulation of subgrade settlement with tonnage when inclusion is installed at the subgrade top and when thicker subballast is used.

Considering a 1 km long typical ballasted railway track section, where the subballast layer has a top width of 7 m and side slope of 2:1 (H:V), the estimated quantity of material required for constructing a 0.2 m thick subballast layer is approximately 2841.6 tons. Based on an emission factor of 5.2 kg CO_2e per ton for natural quarried gravel [87,88], the total carbon footprint associated with this layer is estimated at 14.78 tons CO_2e. The incorporation of cellular geoinclusions allows for a reduction in subballast thickness to 0.15 m, resulting in materials saved that correspond to a reduction of approximately 3.84 tons CO_2e per km of railway track. It must be noted that the use of cellular inclusions introduces its own embodied carbon footprint. Due to a lack of comprehensive data on the embodied emissions of cellular inclusions, the net reduction in carbon footprint cannot be precisely quantified. Estimation of this value remains a subject of future research.

3.6.5. Influence of Material Type

The amount of confinement offered by cellular artificial inclusions depends on the material with which they are manufactured [40]. Therefore, the material type can significantly affect the magnitude of cumulated settlement in a reinforced track. In the present study, four types of inclusion materials are considered, viz., rubber tire, polypropylene (PP) geocomposite (biaxial geogrid with fabric), HDPE, and coir geotextile (refer to Figure 16a

for their load vs. strain curves obtained by [89–92]). Figure 16b shows a comparison of track settlement accumulated after a tonnage of 15 MGT between unreinforced track and track that was reinforced using artificial inclusions manufactured from different types of materials. It is apparent that the incorporation of artificial inclusions manufactured using different types of materials improves the performance of ballasted railway track by reducing track settlement. It can also be observed from the figure that the magnitude of settlement reduction varies with material type. The discarded rubber tire provides the maximum decrease in settlement (33%), followed by PP geocomposites (30.6%), HDPE (22.6%), and coir geotextile (12.7%). This is attributed to the fact that the amount of additional confinement depends on the mobilized modulus of inclusion. Since rubber tire has the highest modulus (refer to Figure 16a), it provides maximum confinement, followed by PP geocomposites, HDPE and coir geotextile.

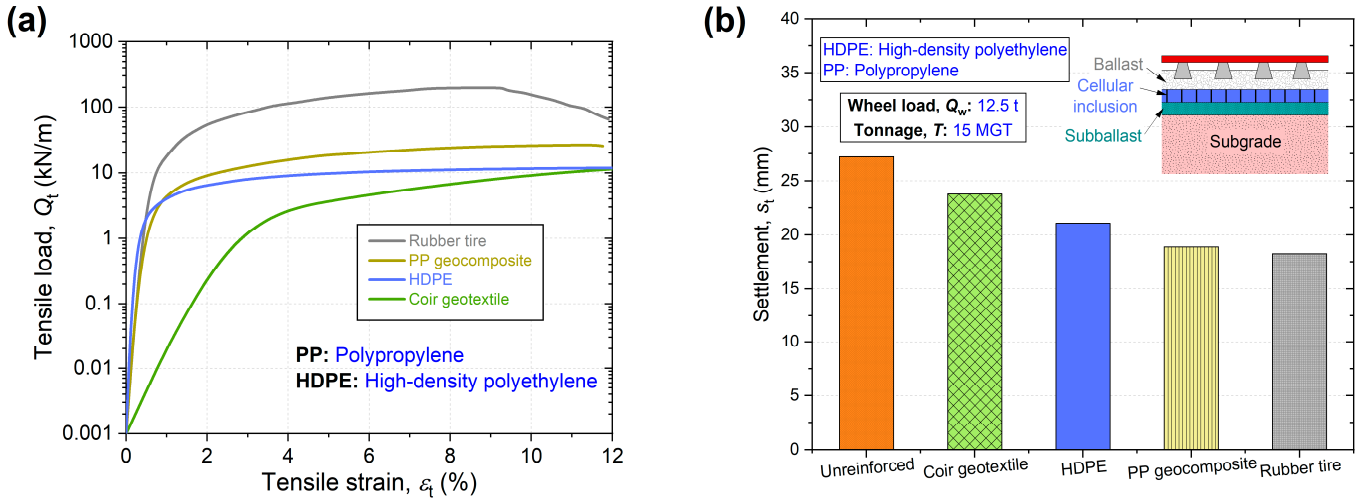

Figure 16. (**a**) Load versus strain relationship for various artificial inclusion materials (modified after [30]); (**b**) Comparison of track settlement for unreinforced and reinforced ballasted track.

3.7. Limitations and Future Scope

The bending of cellular inclusion walls under vertical loading was not considered in this study. This simplification could affect the accuracy of the estimated additional confinement provided by the inclusions, potentially influencing the predicted track response. Future studies shall refine the confinement model by incorporating the bending behavior to improve the accuracy of predictions. In addition, field investigations are recommended to assess the performance of railway tracks, incorporating these inclusions, in real-world conditions.

3.8. Concluding Remarks

This section investigated the effectiveness of cellular artificial inclusions in enhancing the performance and sustainability of a ballasted railway track using a computational methodology that integrated a rheological track model with a confinement model for artificial inclusions. The main findings from this section are as follows:

- Incorporating cellular artificial inclusions in a ballasted track curtailed the cumulative settlement by up to 33% after 15 MGT, depending on the material type.
- Reinforced tracks required a smaller quantity of natural aggregates to achieve subgrade performance comparable to that in unreinforced tracks. This reduction in material usage could lead to substantial cost savings and lower carbon emissions associated with the extraction, processing, and transportation of natural aggregates.

- The cellular inclusions remained effective at elevated load levels, making them a sustainable solution for enhancing the resilience of railway infrastructure against future load escalation.

These findings highlight that the use of cellular artificial inclusions in ballasted railway tracks significantly enhances their performance and contributes towards sustainability in the following ways:

- Reducing the cumulative track settlement, which minimizes the need for frequent maintenance.
- Enhancing the capacity of tracks to support increased loading from heavy haul trains.
- Lowering the quantity of natural quarried material required for their construction.

These benefits collectively reduce the carbon footprint of railway tracks by cutting down emissions associated with maintenance activities, as well as the extraction, processing, and transportation of quarried materials. In addition, the results indicate that discarded tires, either whole or in aggregate form, can improve track performance. This approach not only curtails the reliance on natural resources but also helps divert waste away from landfills and stockpiles. The subsequent section explores how planar inclusions can enhance the sustainability of railway tracks.

4. Using Planar Artificial Inclusions in Railway Embankments

4.1. General

Planar artificial inclusions can be installed at the base of pile-supported embankments (PSE) to enhance their performance and sustainability. These embankments are typically used in areas where subgrade soil possesses unfavorable engineering characteristics, such as high compressibility and low shear strength. In PSEs, the fill material shows higher settlement between the piles due to the stiffness differences [93]. However, a shear resistance mechanism, called soil arching, is developed within the fill, which limits this settlement, and most of the train-induced load is transferred to the piles [94,95]. The incorporation of planar inclusions could improve this load-transfer mechanism by virtue of the tensioned-membrane effect [46].

Several studies have explored the effect of planar inclusions on the load-transfer behavior in PSE. Cao et al. [47] conducted model tests to study the effect of factors such as relative settlement between subsoil and piles, height of embankment, and clear pile spacing on the soil arching mechanism. Their findings revealed that soil arching was completely mobilized when the relative settlement between the pile and subsoil reaches 6 to 8 mm. Moreover, differential settlement decreased as the embankment height to clear pile spacing ratio increased. The use of a planar inclusion further enhanced the soil arching effect. Lang et al. [48] performed 3D FE analyses to study the long-term load transfer mechanism in pile-supported highway embankments under traffic-induced loading. Their results indicated that factors such as traffic loading type, vehicle speed, pile spacing, and the number of inclusion layers substantially influence the load distribution over time.

Pan et al. [96] carried out field tests to monitor the evolution of soil arching and deformation in soil, piles, and planar inclusions during both the construction and equilibrium phases of embankments. Their findings suggested that three stages of soil arching evolution occurred with increasing fill height. Soil arching was completely mobilized when the pile–soil settlement ratio attained a minimum value, corresponding to a differential settlement of approximately 1% of the net pile spacing. Strain in inclusions primarily developed in the early stage of filling, with a progressive reduction in strain accumulation during subsequent filling stages. Ye et al. [49] conducted numerical analyses on various pile layouts and found that a triangular arrangement enhanced the load transfer mecha-

nism. Furthermore, in multi-layered inclusions, the bottom layer played a critical role in load distribution. Li et al. [97] investigated the load-transfer behavior in PSE through a modified FE model, which was validated using field test data. Their findings revealed that pile spacing significantly influenced load-transfer behavior in PSE, thereby affecting the long-term performance and sustainability of railway infrastructure.

This review of existing studies suggests that integrating planar inclusion layers in PSE can improve their performance and contribute to sustainability by reducing the number of piles required. However, limited research has focused on the impact of train loading on the tensile stresses in planar inclusions and the load-transfer mechanisms. Therefore, the next section investigates the effectiveness of a planar artificial inclusion, specifically a geogrid, in enhancing the soil arching within a PSRE.

4.2. Numerical Modelling of Pile-Supported Embankment

A pile-supported embankment with and without a planar inclusion layer was analyzed under two-dimensional (2D) plane strain conditions using the FE method. Figure 17 presents a schematic representation of a pile-supported railway embankment (PSRE) with a planar inclusion layer at the bottom, highlighting the soil arches and the modelled region. The spacing (s) and diameter (d) of the piles were chosen as 2–3.5 m and 1 m, respectively, and these piles extended to a depth of 8 m in the subsoil. The height of the embankment (h_e), incorporating a 0.4 m thick gravel layer, was considered to be 3.5 m. The planar inclusion was a PP biaxial geogrid with a stiffness of 1 kN/m, which was embedded at the mid-depth (0.2 m) of the gravel layer. To simulate train-induced loads and the weight of the railway track, an equivalent dynamic loading was exerted on the embankment surface. The bottom and side boundaries of the FE model were constrained, with the bottom fully fixed and the sides normally fixed [98]. Table 3 summarizes the values of material parameters employed in the numerical simulations to investigate the load-transfer behavior in PSRE.

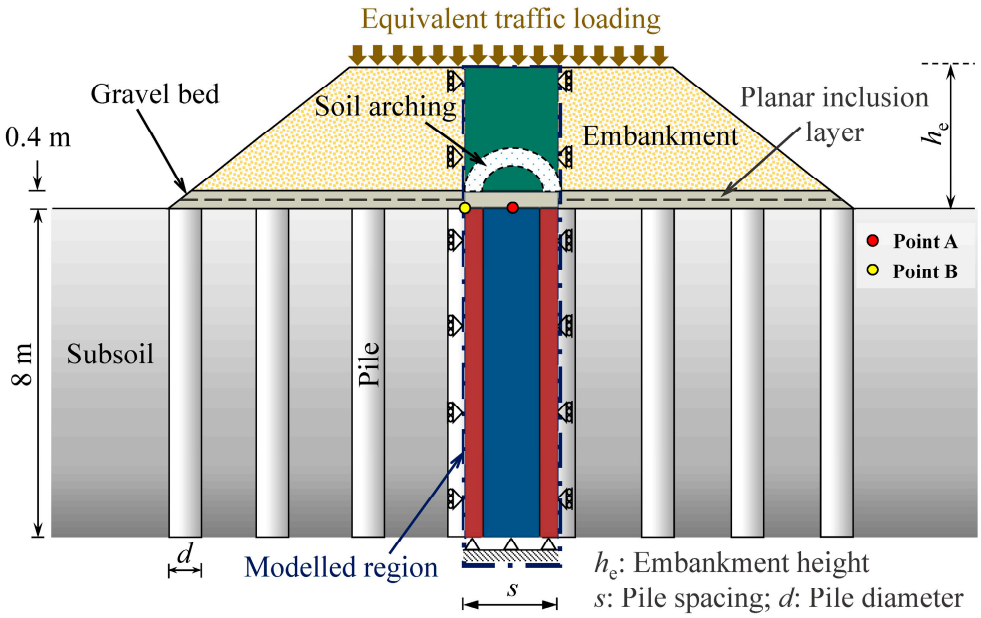

Figure 17. Schematic representation of a pile supported railway embankment (PSRE), highlighting the soil arching effect and the modelled region (modified after [64]).

Table 3. Material parameters used in numerical simulations to investigate the load-transfer behavior in PSRE (data sourced from [99]).

Material	Density, ρ (kg/m^3)	Young's Modulus, E (MN/m^2)	Cohesion, c' (kN/m^2)	Friction Angle, ϕ' (°)
Embankment fill	2041	20	0.1	30
Gravel bed	2143	25	0.1	35
Subsoil	1877	10	8	22
Pile	2449	20×10^3	-	-
PP biaxial geogrid #	-	500	-	-

(at 2% tensile strain).

Eight-noded, quadratic solid elements (CPE8R) with reduced integration were used for discretizing the FE model of PSRE. The interaction between soil and pile was modelled using a "hard" normal contact and a penalty-based tangential contact with a friction coefficient of 0.7. The FE modelling process began with the application of geostatic loading to generate the initial stresses in the subsoil, followed by sequential construction of the gravel bed, rigid piles, and embankment. Once full geometry was created, an equivalent dynamic-load-simulating railway track self-weight and train movement was exerted on the embankment surface.

Detailed information on the 3D to 2D conversion method, applied loading and model validation is available elsewhere (see, for, e.g., [99]). In the present study, the influence of embankment fill parameters, including h_e, elastic modulus (E_e), effective friction angle (ϕ'), and pile spacing (s) on the soil arching mechanism and tensile stresses generated in the planar inclusion is investigated.

4.3. Results and Discussion

Figure 18 illustrates the effect of pile spacing on the settlement in embankment fill. In the absence of reinforcement, the settlement at Point A (at D_{td} = 0) increases from 6.3 to 12 mm as s increases from 2 to 3.5 m. To mitigate this settlement, a planar inclusion layer can be introduced at the mid-depth of the gravel bed. This inclusion reduces the vertical stress at Point A (see Figure 19) by virtue of the tensioned membrane effect and consequently decreases the settlement.

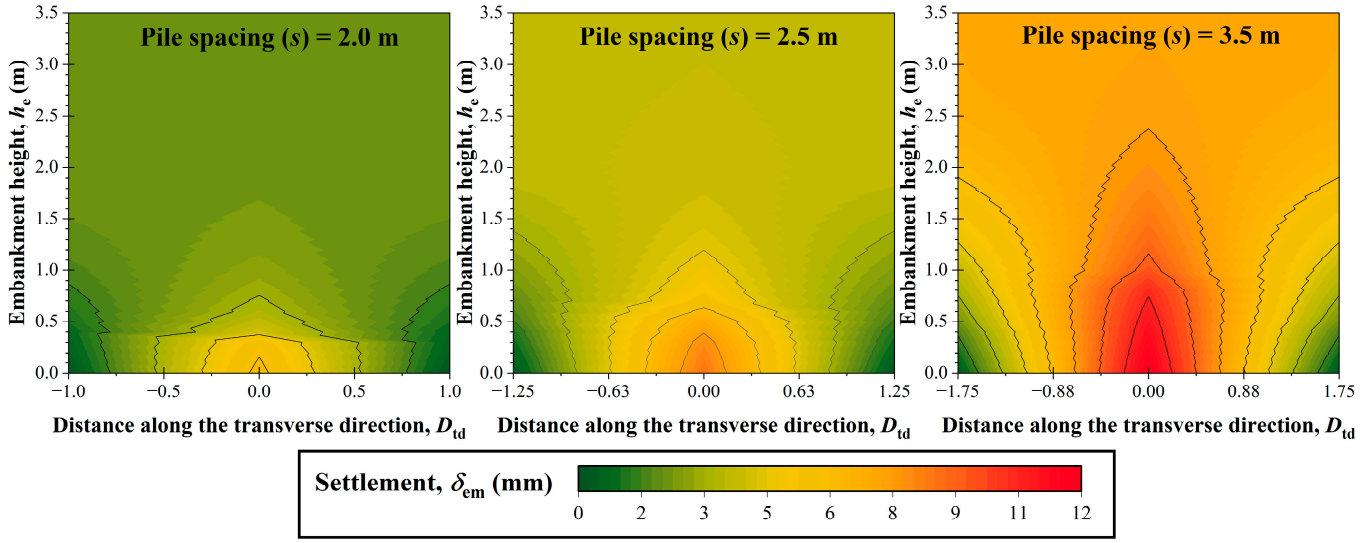

Figure 18. Settlement in embankment fill at different pile spacing for the unreinforced case.

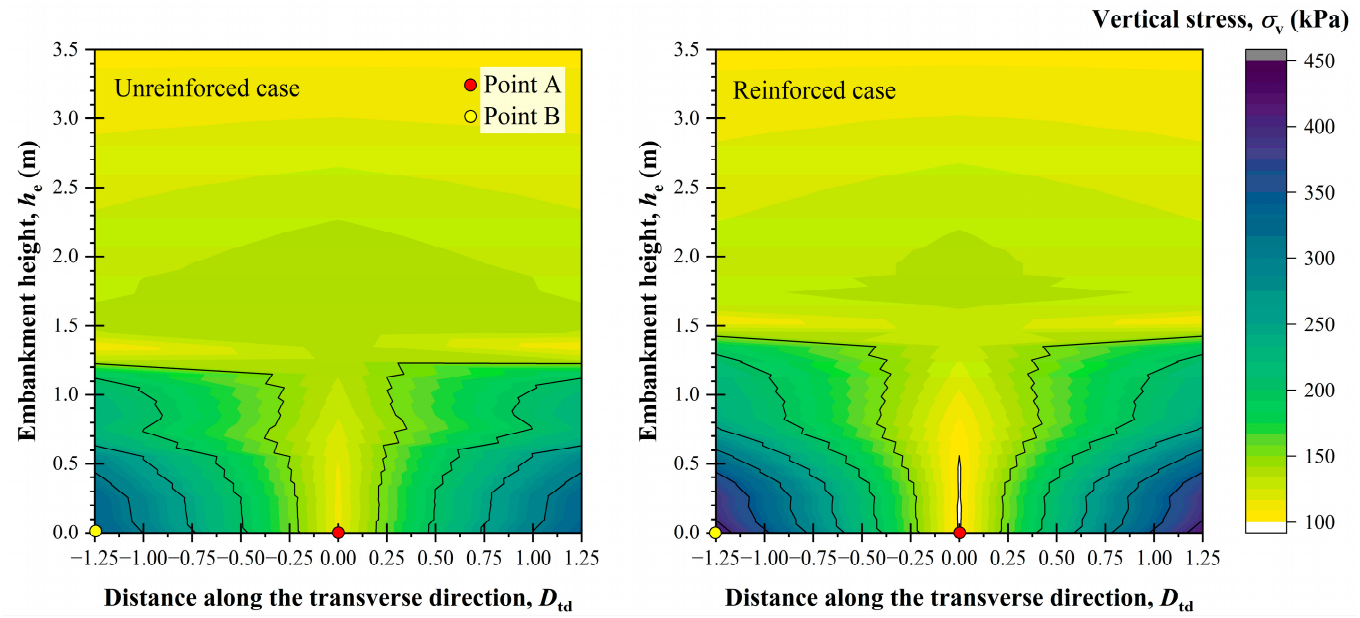

Figure 19. Vertical stress distribution contours in embankment for unreinforced and reinforced cases.

Figure 19 illustrates the vertical stress distribution contours for both a conventional embankment (i.e., without inclusion layer) and the one reinforced with a planar inclusion layer. These contours represent the transmission of vertical stresses from the top to the base of the embankment. It must be noted that the height of the embankment and spacing of piles for this analysis are set at 3.5 and 2.5 m, respectively.

It can be seen in Figure 19 that the vertical stress for the unreinforced case initially increases from h_e = 3.5 to 2 m and then decreases from 2 to 0.5 m along a section passing through point A. Meanwhile, the vertical stress progressively increases from the embankment top to the bottom along a section passing through point B. Thus, the vertical stress within the embankment fluctuates, decreasing at Point A and increasing at Point B, within the height range of 0.5 to 2 m. This region is referred to as the load transfer zone.

For the reinforced case, the vertical stress distribution follows a similar trend to that of the unreinforced case. However, a notable difference is observed in the magnitude of vertical stress at key points. At point A, the vertical stress is reduced by approximately 10%, whereas at point B, it is elevated by 19% compared to the unreinforced case. This variation is primarily ascribed to the development of tensile forces within the inclusion layer, which enhances load redistribution and improves the efficiency of the load-transfer mechanism.

It is apparent from Figure 20 that the use of planar inclusions reduces the settlement at the embankment top by around 43% at a pile spacing of 2.5 mm. A similar reduction in settlement with the incorporation of inclusions was reported in [100,101]. It is important to note that by using planar inclusions in the base of PSRE, it is feasible to increase the spacing of the piles without compromising the embankment performance, as illustrated in Figure 20. It is evident from the figure that the settlement at the embankment crest with 2 m pile spacing (unreinforced case) is similar to the reinforced case with a 2.5 m pile spacing. This indicates that similar performance can be achieved with wider pile spacing when planar inclusions are used, implying fewer piles are needed. This could potentially reduce the amount of concrete required as well as lower the carbon footprint and overall construction cost.

Figure 21 illustrates the formation of soil arches within the embankment, highlighting both their outer and inner boundaries. To depict the shape of the soil arch, multiple vertical planes perpendicular to the transverse direction are analyzed. The heights corresponding

to the minimum and maximum vertical stresses along each vertical plane define the inner and outer boundaries of the soil arch, respectively.

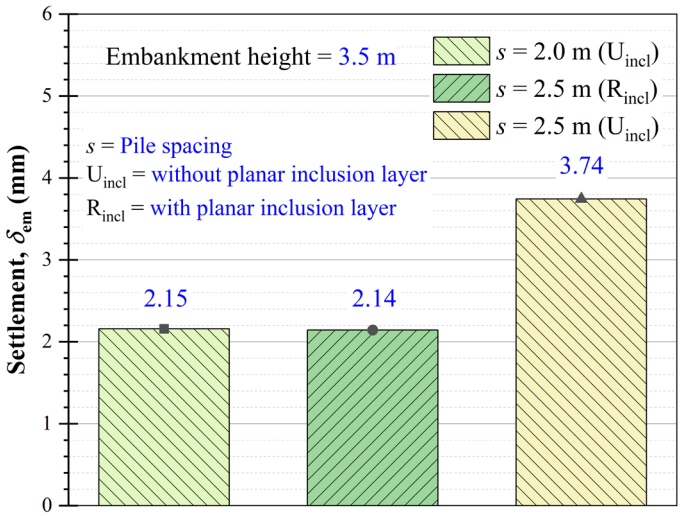

Figure 20. Variation in settlement with and without planar inclusions for different pile spacing.

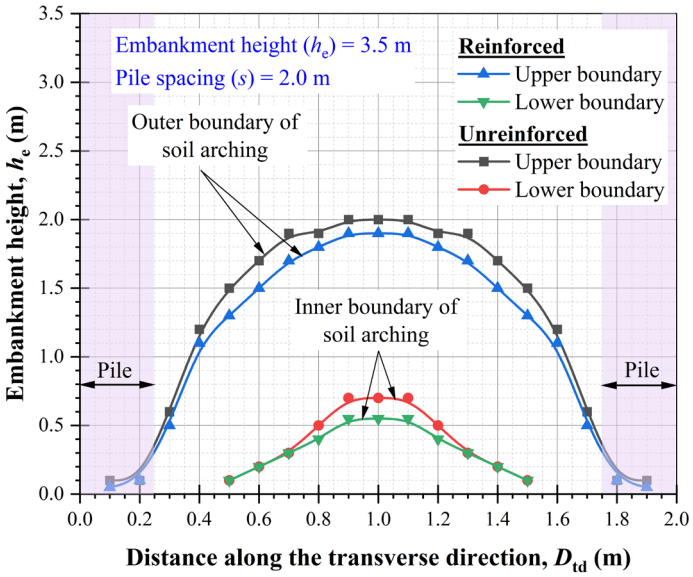

Figure 21. Formation of soil arch in a reinforced and unreinforced railway embankment.

In an unreinforced embankment, at a section along point A (see Figure 17), the maximum vertical stress corresponding to the outer boundary of the soil arch is observed at h_e = 2 m. Meanwhile, the inner boundary of the soil arch is identified at a height of 0.7 m, resulting in a load transfer zone of 1.3 m. This zone becomes thinner along the section at point B and deviates from the semicircular arching pattern proposed by Hewlett and Randolph [93]. Instead, it aligns more closely with the multi-shell arching theory suggested by Kempfert et al. [102], indicating a more complex load redistribution mechanism.

In the reinforced case, a similar trend is observed, with a 5% increase in the load transfer zone at a section along point A. This indicates that the reinforcement effectively improves stress distribution within the embankment without altering the fundamental arching behavior. This observation is ascribed to the tensioned membrane effect, wherein the inclusion layer mobilizes tensile forces that counteract vertical deformation. However, the magnitude of tension in the inclusion layer depends on various factors, including the stiffness and tensile strength of the material, depth and position of the inclusions within

the granular bed, the spacing and geometry of piles, and the characteristics of the overlying embankment fill. These parameters collectively govern the extent to which inclusions can redistribute stress and reduce settlement.

Figure 22 illustrates how tension developed in the inclusions (T_{pi}) varies with the properties of embankment fill material, such as elastic modulus (E_e) and friction angle (ϕ'). The results indicate that as E_e increases from 10 to 30 MPa, the tensile stresses in the inclusions significantly decrease by up to 35%. Similarly, an increase in ϕ' from 25° to 45° leads to a reduction in T_{pi} by approximately 54%. This reduction in tension can be ascribed to the improved strength and stiffness of the embankment fill, which minimizes settlement, and consequently, the demand for planar reinforcement. These findings suggest that when E_e and ϕ' are sufficiently high, the contribution of inclusions to load transfer is diminished. Therefore, planar reinforcement is more effective for embankments constructed using fill with a smaller modulus and friction angle.

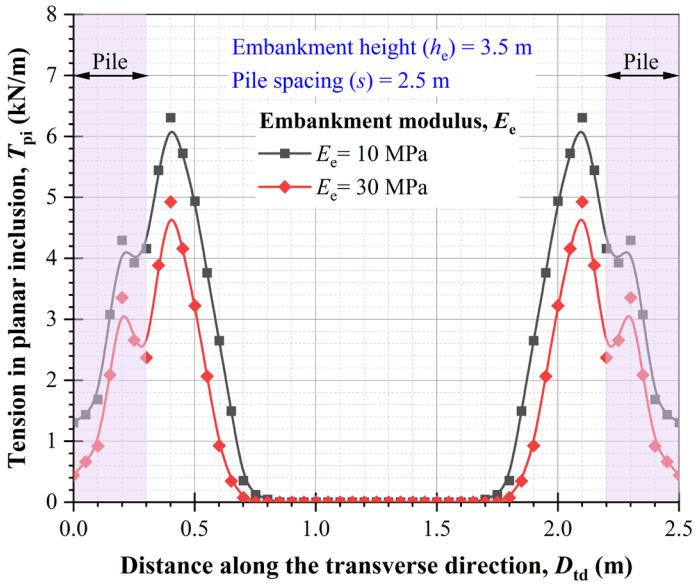

(**a**)

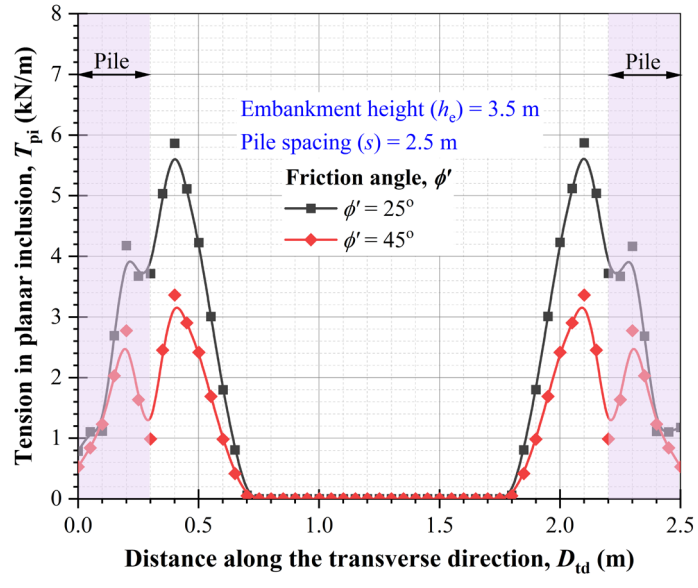

(**b**)

Figure 22. Effect of (**a**) elastic modulus; (**b**) effective friction angle of fill material on tension in planar inclusion layer (modified after [64]).

4.4. Limitations and Future Scope

In this study, a 2D FE method was employed to investigate the behavior of pile-supported railway embankments with planar artificial inclusions. While the 2D FE approach provides reasonably accurate predictions more quickly than 3D FE analysis, it is unable to capture the influence of factors such as embankment slope, moving loads, and non-uniform stress-distribution within the inclusion layer. Future studies shall address this limitation by using 3D FE analysis, which can more accurately predict the performance of pile-supported railway embankments under realistic geometry and loading conditions.

4.5. Concluding Remarks

This section investigated the effectiveness of a planar artificial inclusion in enhancing the load transfer mechanism within a pile-supported railway embankment (PSRE) using 2D FE analysis. The main findings from this section are as follows:

- The incorporation of planar inclusions at the base of the PSRE improved the load-transfer mechanism by reducing the magnitude of stress transmitted to the subsoil. This improvement is primarily attributed to the tensioned membrane effect within the inclusion layer, which facilitates better load distribution and reduces differential settlement.
- The use of planar inclusions could reduce the number of piles required for PSRE construction, thereby curtailing the carbon emissions associated with piling operations.
- By reinforcing the embankment, the inclusion layer effectively mobilizes soil arching, leading to enhanced stability and long-term performance of the railway track. This improvement not only optimizes structural performance but could also contribute to the sustainability of transport infrastructure by minimizing maintenance needs and extending service life.

5. Conclusions

This study assessed the effectiveness of three approaches in enhancing the performance and sustainability of railway track infrastructure: (a) a novel composite material comprising soil, aggregates derived from discarded rubber tires and PFA; (b) cellular artificial inclusions; (c) planar artificial inclusions.

Laboratory investigations revealed that the soil–rubber–PFA composite exhibits excellent mechanical performance, including low residual strain (0.29–0.98%), minimal pore water pressure (~1–10 kPa), adequate damping and high permeability (~5.9×10^{-5} m/s). Its use would promote sustainability by repurposing scrap tires and substituting carbon-intensive cement with PFA, thereby reducing environmental impact while meeting engineering requirements for ballastless track applications.

Results from a rheological computational approach highlighted that the use of cellular artificial inclusions could significantly reduce cumulative settlement (by up to 33%) and material usage in ballasted railway tracks. This could potentially lead to lower maintenance requirements and reduced carbon emissions. Their effectiveness under higher load levels demonstrates their potential for enhancing the resilience of railway infrastructure against future load escalation.

Finite element analyses of pile-supported railway embankments showed that planar artificial inclusions improve the load transfer to the piles through the tensioned membrane effect and reduce the subsoil stress and settlement. Their use enabled wider pile spacing, which could lead to fewer piles, lower concrete usage and reduced carbon emissions, without compromising the stability of the PSRE.

These techniques show strong potential for enhancing the long-term resilience and sustainability of railway infrastructure. Their integration into future designs could enable

high-performing systems with lower carbon footprints as well as greater adaptability to future load escalation and climate-related impacts.

Author Contributions: Conceptualization, S.N.; methodology, S.N., P.P., M.A.F. and N.K.M.; validation, S.N., P.P., M.A.F. and N.K.M.; formal analysis, P.P., M.A.F. and N.K.M.; investigation, S.N., P.P., M.A.F. and N.K.M.; resources, S.N.; data curation, P.P., M.A.F. and N.K.M.; writing—original draft preparation, P.P., M.A.F. and N.K.M.; writing—review and editing, S.N.; visualization, S.N., P.P., M.A.F. and N.K.M.; supervision, S.N.; project administration, S.N.; funding acquisition, S.N. All authors have read and agreed to the published version of the manuscript.

Funding: This research received no external funding.

Institutional Review Board Statement: Not applicable.

Informed Consent Statement: Not applicable.

Data Availability Statement: The data presented in this study are available on reasonable request from the corresponding author.

Acknowledgments: This study was a part of doctoral research by P.P., M.A.F. and N.K.M. P.P. and N.K.M. wish to thank the UTS eResearch team for granting access to the interactive high-performance computing facility. The authors wish to thank the reviewers for their suggestions and comments to improve the technical merit of this study.

Conflicts of Interest: Author Naveen Kumar Meena was employed by the company Beca Pty Ltd. The remaining authors declare that the research was conducted in the absence of any commercial or financial relationships that could be construed as a potential conflict of interest.

Abbreviations

The following abbreviations have been used in this manuscript:

2D, 3D	Two and three-dimensional, respectively
CDSS	Cyclic direct simple shear
CSL	Critical state line
DE	Discrete element
FE	Finite element
GSD	Grain size distribution
HDPE	High-density polyethylene
MGT	Million gross metric tons
PFA	Polyurethane foam adhesive
PP	Polypropylene
PSE	Pile-supported embankments
PSR	Principal stress rotation
PSRE	Pile-supported railway embankment
SDSS	Static direct simple shear

Appendix A

The constitutive parameters for the plastic slider elements for substructure layers are provided in Tables A1 and A2. The constitutive relations for ballast, subballast and subgrade slider elements are based on modified Nor-Sand and characteristic stress-based models. The details of these models can be found elsewhere [81].

Table A3 lists the constitutive parameters for the plastic slider elements for ballast and subgrade layers used in the validation.

Table A1. Parameters for slider elements for ballast and subballast layers (data sourced from [30]).

Parameter	Symbol	Ballast	Subballast
Reference void ratio on the critical state line (CSL)	Γ	1.4	0.9
Critical stress ratio	M_{tc}	1.25	1.15
Volumetric coupling parameter	N_v	0.2	0.3
Slope of the CSL	λ	0.1	0.05
State-dilatancy parameter	χ_{tc}	3	4.2
Plastic hardening parameter	H	50-(250ψ)	160-(260ψ)
Cyclic hardening parameter	a_h	0.3	0.185
Plastic softening parameter	Z	10	20

Note: ψ is state parameter.

Table A2. Parameters for slider elements for subgrade layer (data sourced from [30]).

Parameter	Symbol	Value
Critical state friction angle (°)	φ_c	36
Characteristic stress parameter	ξ	0.1
Slope of the CSL	λ	0.0041
Slope of swelling line	κ	0.002
Spacing parameter	A	0.1
Cyclic hardening parameter	a_h	0.03
Parameter to account for principal stress rotation (PSR) effect	$s_{1\alpha}$	0.7
Parameter to account for PSR effect	$s_{2\alpha}$	0.05

Table A3. Parameters for slider elements used in the validation (data sourced from [30]).

Layer	Parameter	Symbol	Value
Ballast	Reference void ratio on the critical state line (CSL)	Γ	1.4
	Critical stress ratio	M_{tc}	1.42
	Volumetric coupling parameter	N_v	0.2
	Slope of the CSL	λ	0.1
	State-dilatancy parameter	χ_{tc}	3
	Plastic hardening parameter	H	50-(250ψ)
	Cyclic hardening parameter	a_h	0.32
Subgrade	Critical state friction angle (°)	φ_c	42.5
	Characteristic stress parameter	ξ	0.1
	Slope of the CSL	λ	0.0041
	Slope of swelling line	κ	0.002
	Spacing parameter	A	0.1
	Cyclic hardening parameter	a_h	0.09

Note: ψ is state parameter.

References

1. Lawrence, M.; Bullock, R. *The Role of Rail in Decarbonizing Transport in Developing Countries*; World Bank: Washington, DC, USA, 2022.
2. Ahsan, N.; Hewage, K.; Razi, F.; Hussain, S.A.; Sadiq, R. A critical review of sustainable rail technologies based on environmental, economic, social, and technical perspectives to achieve net zero emissions. *Renew. Sustain. Energy Rev.* **2023**, *185*, 113621. [CrossRef]
3. Bressi, S.; Santos, J.; Giunta, M.; Pistonesi, L.; Lo Presti, D. A comparative life-cycle assessment of asphalt mixtures for railway sub-ballast containing alternative materials. *Resour. Conserv. Recycl.* **2018**, *137*, 76–88. [CrossRef]
4. Kiani, M.; Parry, T.; Ceney, H. Environmental life-cycle assessment of railway track beds. *Proc. Inst. Civ. Eng. Eng. Sustain.* **2008**, *161*, 135–142. [CrossRef]

5. Punetha, P.; Nimbalkar, S. Utilisation of construction and demolition waste and recycled glass for sustainable flexible pavements: A critical review. *Transp. Geotech.* **2025**, *54*, 101612. [CrossRef]
6. Pelisser, F.; Zavarise, N.; Longo, T.A.; Bernardin, A.M. Concrete made with recycled tire rubber: Effect of alkaline activation and silica fume addition. *J. Clean. Prod.* **2011**, *19*, 757–763. [CrossRef]
7. Song, W.; Huang, B.; Shu, X.; Wu, H.; Gong, H.; Han, B.; Zou, J. Improving Damping Properties of Railway Ballast by Addition of Tire-Derived Aggregate. *Transp. Res. Rec.* **2019**, *2673*, 299–307. [CrossRef]
8. Garga, V.K.; O'Shaughnessy, V. Tire-reinforced earthfill. Part 1: Construction of a test fill, performance, and retaining wall design. *Can. Geotech. J.* **2000**, *37*, 75–96. [CrossRef]
9. Forsyth, R.A.; Egan, J.P. Use of waste materials in embankment construction. *Transp. Res. Rec.* **1976**, *593*, 3–8.
10. Edil, T.B.; Bosscher, P.J. *Development of Engineering Criteria for Shredded Waste Tires in Highway Applications*; Wisconsin Department of Transportation: Madison, WI, USA, 1992.
11. Sol-Sánchez, M.; Thom, N.H.; Moreno-Navarro, F.; Rubio-Gámez, M.C.; Airey, G.D. A study into the use of crumb rubber in railway ballast. *Constr. Build. Mater.* **2015**, *75*, 19–24. [CrossRef]
12. Epps, J.A. *Uses of Recycled Rubber Tires in Highways*; Transportation Research Board: Washington, DC, USA, 1994; Volume 198.
13. Lamour, M.; Cecchin, A. Repurposed materials in construction: A review of low-processed scrap tires in civil engineering applications for disaster risk reduction. *Constr. Build. Mater.* **2021**, *293*, 123368. [CrossRef]
14. Yoon, Y.W.; Cheon, S.H.; Kang, D.S. Bearing capacity and settlement of tire-reinforced sands. *Geotext. Geomembr.* **2004**, *22*, 439–453. [CrossRef]
15. Bosscher, P.J.; Edil, T.B.; Kuraoka, S. Design of highway embankments using tire chips. *J. Geotech. Eng.* **1997**, *123*, 295–304. [CrossRef]
16. Ahn, I.S.; Cheng, L. Tire derived aggregate for retaining wall backfill under earthquake loading. *Constr. Build. Mater.* **2014**, *57*, 105–116. [CrossRef]
17. Kaushik, M.K.; Kumar, A.; Bansal, A. Performance assessment of gravel–tire chips mixes as drainage layer materials using real active MSW landfill leachate. *Geotech. Geol. Eng.* **2015**, *33*, 1081–1098. [CrossRef]
18. Hidalgo-Signes, C.; Garzón-Roca, J.; Grima-Palop, J.M.; Insa-Franco, R. Use of rubber shreds to enhance attenuation of railway sub-ballast layers made of unbound aggregates. *Mater. Constr.* **2017**, *67*, 115. [CrossRef]
19. Meles, D.; Bayat, A.; Soleymani, H. Compression Behavior of Large-Sized Tire-Derived Aggregate for Embankment Application. *J. Mater. Civ. Eng.* **2013**, *25*, 1285–1290. [CrossRef]
20. Mills, B.; McGinn, J. Design, Construction, and Performance of a Highway Embankment Failure Repaired with Tire-Derived Aggregate. *Transp. Res. Rec.* **2010**, *2170*, 90–99. [CrossRef]
21. Sadeghi, J.; Toloukian, A.; Zarei, M.A.; Khani, N. Improvement of ballast behavior by inclusion of tire-derived aggregates with optimum size. *Constr. Build. Mater.* **2025**, *458*, 139530. [CrossRef]
22. Gong, H.; Song, W.; Huang, B.; Shu, X.; Han, B.; Wu, H.; Zou, J. Direct shear properties of railway ballast mixed with tire derived aggregates: Experimental and numerical investigations. *Constr. Build. Mater.* **2019**, *200*, 465–473. [CrossRef]
23. Wolfe, S.L.; Humphrey, D.N.; Wetzel, E.A. Development of tire shred underlayment to reduce groundborne vibration from LRT track. In *Geotechnical Engineering for Transportation Projects*; GeoTrans: Los Angeles, CA, USA, 2004; pp. 750–759.
24. Guo, Y.; Ji, Y.; Zhou, Q.; Markine, V.; Jing, G. Discrete Element Modelling of Rubber-Protected Ballast Performance Subjected to Direct Shear Test and Cyclic Loading. *Sustainability* **2020**, *12*, 2836. [CrossRef]
25. Esmaeili, M.; Aela, P.; Hosseini, A. Experimental assessment of cyclic behavior of sand-fouled ballast mixed with tire derived aggregates. *Soil Dyn. Earthq. Eng.* **2017**, *98*, 1–11. [CrossRef]
26. Khoshoei, S.M.; Bak, H.M.; Abtahi, S.M.; Hejazi, S.M.; Shahbodagh, B. Experimental Investigation of the Cyclic Behavior of Steel-Slag Ballast Mixed with Tire-Derived Aggregate. *J. Mater. Civ. Eng.* **2021**, *33*, 04020468.
27. Sun, Q.; Indraratna, B.; Grant, J. Numerical Simulation of the Dynamic Response of Ballasted Track Overlying a Tire-Reinforced Capping Layer. *Front. Built Environ.* **2020**, *6*, 6. [PubMed]
28. Zhou, H.; Wen, X. Model studies on geogrid-or geocell-reinforced sand cushion on soft soil. *Geotext. Geomembr.* **2008**, *26*, 231–238. [CrossRef]
29. Leshchinsky, B.; Ling, H. Effects of geocell confinement on strength and deformation behavior of gravel. *J. Geotech. Geoenviron. Eng.* **2013**, *139*, 340–352. [CrossRef]
30. Punetha, P.; Nimbalkar, S. Performance improvement of ballasted railway tracks using three-dimensional cellular geoinclusions. *Geotext. Geomembr.* **2022**, *50*, 1061–1082. [CrossRef]
31. Chrismer, S. *Test of Geoweb to Improve Track Stability over Soft Subgrade*; TD 97-045; Association of American Railroads: Washington, DC, USA, 1997.
32. Giroud, J.P.; Han, J. Design method for geogrid-reinforced unpaved roads. I. Development of design method. *J. Geotech. Geoenviron. Eng.* **2004**, *130*, 775–786. [CrossRef]

33. Cheng, B.; Huang, J.; Wang, H.; Li, X. Influences of Geocell Reinforcement on Shear Strength of Railway Roadbeds. *Transp. Res. Rec.* **2024**, *2678*, 1029–1045. [CrossRef]
34. Zarembski, A.M.; Palese, J.; Hartsough, C.M.; Ling, H.I.; Thompson, H. Application of geocell track substructure support system to correct surface degradation problems under high-speed passenger railroad operations. *Transp. Infrastruct. Geotech.* **2017**, *4*, 106–125. [CrossRef]
35. Kaewunruen, S.; Remennikov, A.M.; Nguyen, P.; Aikawa, A. Field performance to mitigate impact vibration at railway bridge ends using soft baseplates. In Proceedings of the 11th World Congress on Railway Research, Milan, Italy, 30 May–1 June 2016; pp. 1–10.
36. Nimbalkar, S.; Punetha, P.; Kaewunruen, S. Performance improvement of ballasted railway tracks using geocells: Present state of the art. In *Geocells. Springer Transactions in Civil and Environmental Engineering*; Sitharam, T.G., Hegde, A., Kolathayar, S., Eds.; Springer: Singapore, 2020.
37. Pokharel, S.K.; Han, J.; Leshchinsky, D.; Parsons, R.L.; Halahmi, I. Investigation of factors influencing behavior of single geocell-reinforced bases under static loading. *Geotext. Geomembr.* **2010**, *28*, 570–578. [CrossRef]
38. Mengelt, M.; Edil, T.B.; Benson, C.H. Resilient modulus and plastic deformation of soil confined in a geocell. *Geosynth. Int.* **2006**, *13*, 195–205. [CrossRef]
39. Satyal, S.R.; Leshchinsky, B.; Han, J.; Neupane, M. Use of cellular confinement for improved railway performance on soft subgrades. *Geotext. Geomembr.* **2018**, *46*, 190–205. [CrossRef]
40. Punetha, P.; Nimbalkar, S.; Khabbaz, H. Evaluation of additional confinement for three-dimensional geoinclusions under general stress state. *Can. Geotech. J.* **2020**, *57*, 453–461. [CrossRef]
41. Raymond, G.P. Failure and reconstruction of a gantry crane ballasted track. *Can. Geotech. J.* **2001**, *38*, 507–529. [CrossRef]
42. Liu, H.L.; Ng, C.W.W.; Fei, K. Performance of a Geogrid-Reinforced and Pile-Supported Highway Embankment over Soft Clay: Case Study. *J. Geotech. Geoenviron. Eng.* **2007**, *133*, 1483–1493. [CrossRef]
43. Almeida, M.S.S.; Ehrlich, M.; Spotti, A.P.; Marques, M.E.S. Embankment supported on piles with biaxial geogrids. *Proc. Inst. Civ. Eng. Geotech. Eng.* **2007**, *160*, 185–192. [CrossRef]
44. Esen, A.F.; Woodward, P.K.; Laghrouche, O.; Connolly, D.P. Long-Term Performance Assessment of a Geosynthetic-Reinforced Railway Substructure. *Sustainability* **2023**, *15*, 9364. [CrossRef]
45. Wang, H.-L.; Chen, R.-P.; Liu, Q.-W.; Kang, X. Investigation on geogrid reinforcement and pile efficacy in geosynthetic-reinforced pile-supported track-bed. *Geotext. Geomembr.* **2019**, *47*, 755–766. [CrossRef]
46. Han, J.; Gabr, M.A. Numerical Analysis of Geosynthetic-Reinforced and Pile-Supported Earth Platforms over Soft Soil. *J. Geotech. Geoenviron. Eng.* **2002**, *128*, 44–53. [CrossRef]
47. Cao, W.; Xie, Z.; Yue, Y.; Zhao, M.; Li, Q.; Hu, W. Model tests on 3D soil arching in pile-supported embankments with and without geotextile. *Case Stud. Constr. Mater.* **2024**, *20*, e02783. [CrossRef]
48. Lang, R.; Ma, C.; Sun, L.; Mu, K.; Feng, S.; Cheng, X.; Zhou, L. Investigation of soil arching effect and accumulative deformation in pile-supported embankments subjected to traffic loading using numerical modeling. *Int. J. Geomech.* **2024**, *24*, 04024136. [CrossRef]
49. Ye, G.-B.; Wang, M.; Zhang, Z.; Han, J.; Xu, C. Geosynthetic-reinforced pile-supported embankments with caps in a triangular pattern over soft clay. *Geotext. Geomembr.* **2020**, *48*, 52–61. [CrossRef]
50. Fagundes, D.F.; Almeida, M.S.S.; Thorel, L.; Blanc, M. Load transfer mechanism and deformation of reinforced piled embankments. *Geotext. Geomembr.* **2017**, *45*, 1–10. [CrossRef]
51. Fonseca, E.C.A.; Palmeira, E.M. Evaluation of the accuracy of design methods for geosynthetic-reinforced piled embankments. *Can. Geotech. J.* **2019**, *56*, 761–773. [CrossRef]
52. Punetha, P.; Nimbalkar, S.; Khabbaz, H. Simplified geotechnical rheological model for simulating viscoelasto-plastic response of ballasted railway substructure. *Int. J. Numer. Anal. Methods Geomech.* **2021**, *45*, 2019–2047. [CrossRef]
53. TfNSW. *QA Specification 3051: Granular Pavement Base and Subbase Materials*; Transport for New South Wales: Sydney, Australia, 2020.
54. *Australian Standard AS 1289.3.5.1*; Methods of Testing Soils for Engineering Purposes, Part 3.5.1: Soil Classification Tests—Determination of the Soil Particle Density of a Soil—Standard Method. Standards Australia: Sydney, Australia, 2025.
55. Chip Tyre Supporting Legal Tyre Recycling. Available online: https://chiptyre.com.au/process/ (accessed on 2 September 2025).
56. Farooq, M.A.; Nimbalkar, S. Monotonic and cyclic triaxial testing of untreated and polyurethane-treated soil and soil–rubber mixtures. *Acta Geotech.* **2024**, *19*, 605–630. [CrossRef]
57. Farooq, M.A.; Nimbalkar, S. Novel sustainable base material for concrete slab track. *Constr. Build. Mater.* **2023**, *366*, 130260.
58. Farooq, M.A.; Nimbalkar, S. Static and cyclic performance of polyurethane foam adhesive bound soil–rubber mixtures under drained conditions. *Acta Geotech.* **2024**, *19*, 561–589. [CrossRef]
59. Ding, Y.; Zhang, J.; Chen, X.; Wang, X.; Jia, Y. Experimental investigation on static and dynamic characteristics of granulated rubber-sand mixtures as a new railway subgrade filler. *Constr. Build. Mater.* **2021**, *273*, 121955. [CrossRef]

60. Gómez, J.; Casado, J.A.; Carrascal, I.A.; Diego, S.; Ferreño, D.; Mondragón, C. Experimental Validation of a New Antivibration Elastomeric Material Fabricated from End-of-Life Tires for Slab Track Systems with Embedded Rail. *J. Test. Eval.* **2021**, *49*, 1763–1777. [CrossRef]
61. Huang, J.-J.; Su, Q.; Cheng, Y.-M.; Liu, B.; Liu, T. Improved performance of the subgrade bed under the slab track of high-speed railway using polyurethane adhesive. *Constr. Build. Mater.* **2019**, *208*, 710–722. [CrossRef]
62. Čebašek, T.M.; Esen, A.F.; Woodward, P.K.; Laghrouche, O.; Connolly, D.P. Full scale laboratory testing of ballast and concrete slab tracks under phased cyclic loading. *Transp. Geotech.* **2018**, *17*, 33–40. [CrossRef]
63. Farooq, M.A.; Nimbalkar, S.; Fatahi, B. Three-dimensional finite element analyses of tyre derived aggregates in ballasted and ballastless tracks. *Comput. Geotech.* **2021**, *136*, 104220. [CrossRef]
64. Farooq, M.A.; Meena, N.K.; Punetha, P.; Nimbalkar, S.; Lam, N. Experimental and Computational Analyses of Sustainable Approaches in Railways. *Infrastructures* **2024**, *9*, 53. [CrossRef]
65. Senthen Amuthan, M.; Boominathan, A.; Banerjee, S. Undrained cyclic responses of granulated rubber-sand mixtures. *Soils Found.* **2020**, *60*, 871–885. [CrossRef]
66. Banzibaganye, G.; Vrettos, C. Sand–tyre chips mixtures in undrained and drained cyclic triaxial tests. *Proc. Inst. Civ. Eng. Ground Improv.* **2022**, *175*, 23–33. [CrossRef]
67. Zhang, J.; Yang, N.; Chen, X.; Hu, H.; Wang, X.; Zhang, J. Investigation of the static and dynamic characteristics of TDA-subballast mixtures. *Transp. Geotech.* **2022**, *32*, 100676. [CrossRef]
68. Madhusudhan, B.R.; Boominathan, A.; Banerjee, S. Cyclic Simple Shear Response of Sand–Rubber Tire Chip Mixtures. *Int. J. Geomech.* **2020**, *20*, 04020136. [CrossRef]
69. Rollins, K.M.; Evans, M.D.; Diehl, N.B.; III, W.D.D. Shear Modulus and Damping Relationships for Gravels. *J. Geotech. Geoenviron. Eng.* **1998**, *124*, 396–405. [CrossRef]
70. Kramer, S.L. *Geotechnical Earthquake Engineering*; Prentice Hall: New Jersey, NJ, USA, 1996.
71. Madhusudhan, B.R.; Boominathan, A.; Banerjee, S. Engineering properties of sand–rubber tire shred mixtures. *Int. J. Geotech. Eng.* **2021**, *15*, 1061–1077.
72. Masad, E.; Taha, R.; Ho, C.; Papagiannakis, T. Engineering Properties of Tire/Soil Mixtures as a Lightweight Fill Material. *Geotech. Test. J.* **1996**, *19*, 297–304. [CrossRef]
73. Li, D.; Hyslip, J.; Sussmann, T.; Chrismer, S. *Railway Geotechnics*; Taylor and Francis: Boca Raton, FL, USA, 2016.
74. Nimbalkar, S.; Indraratna, B. Improved performance of ballasted rail track using geosynthetics and rubber shockmat. *J. Geotech. Geoenviron. Eng.* **2016**, *142*, 04016031. [CrossRef]
75. Leshchinsky, B.; Ling, H. Numerical modeling of behavior of railway ballasted structure with geocell confinement. *Geotext. Geomembr.* **2013**, *36*, 33–43. [CrossRef]
76. Punetha, P.; Nimbalkar, S. Numerical investigation on dynamic behaviour of critical zones in railway tracks under moving train loads. *Transp. Geotech.* **2023**, *41*, 101009. [CrossRef]
77. Liu, Y.; Deng, A.; Jaksa, M. Three-dimensional modeling of geocell-reinforced straight and curved ballast embankments. *Comput. Geotech.* **2018**, *102*, 53–65. [CrossRef]
78. Banerjee, L.; Chawla, S.; Dash, S.K. Application of geocell reinforced coal mine overburden waste as subballast in railway tracks on weak subgrade. *Constr. Build. Mater.* **2020**, *265*, 120774. [CrossRef]
79. Liu, Y.; Deng, A.; Jaksa, M. Three-Dimensional Discrete-Element Modeling of Geocell-Reinforced Ballast Considering Breakage. *Int. J. Geomech.* **2020**, *20*, 04020032. [CrossRef]
80. Doyle, N.F. Railway track design: A review of current practice. In *Bureau of Transport Economics*; Australian Government Publishing Service: Canberra, Australia, 1980.
81. Punetha, P.; Nimbalkar, S. Geotechnical rheological modeling of ballasted railway tracks considering the effect of principal stress rotation. *Can. Geotech. J.* **2022**, *59*, 1793–1818. [CrossRef]
82. Simo, J.C.; Hughes, T.J.R. *Computational Inelasticity*; Springer: New York, NY, USA, 1998.
83. Punetha, P.; Nimbalkar, S.; Khabbaz, H. Analytical evaluation of ballasted track substructure response under repeated train loads. *Int. J. Geomech.* **2020**, *20*, 04020093. [CrossRef]
84. Punetha, P. Dynamic Behaviour of Ballasted Railway Track with Special Reference to Transition Zones. Ph.D. Thesis, University of Technology Sydney, Sydney, Australia, 2022.
85. MathWorks Inc. *MATLAB*, version 2021a; MathWorks Inc.: Natick, MA, USA, 2021.
86. Selig, E.T.; Waters, J.M. *Track Geotechnology and Substructure Management*; Thomas Telford: London, UK, 1994.
87. Racusin, J.D.; McArleton, A. *The Natural Building Companion*; Chelsea Green Publishing: White River Junction, VT, USA, 2012.
88. Imteaz, M.; Mohammadinia, A.; Arulrajah, A. Environmental suitability, carbon footprint and cost savings of recycled plastic for railway applications. *Int. J. Sustain. Eng.* **2021**, *14*, 725–734. [CrossRef]
89. Indraratna, B.; Sun, Q.; Grant, J. Behaviour of subballast reinforced with used tyre and potential application in rail tracks. *Transp. Geotech.* **2017**, *12*, 26–36. [CrossRef]

90. Gonzalez-Torre, I.; Calzada-Perez, M.A.; Vega-Zamanillo, A.; Castro-Fresno, D. Damage evaluation during installation of geosynthetics used in asphalt pavements. *Geosynth. Int.* **2014**, *21*, 377–386. [CrossRef]
91. Biabani, M.M. Behaviour of geocell-reinforced subballast under cyclic loading in plane strain condition. Ph.D. Thesis, University of Wollongong, Wollongong, Australia, 2015.
92. Lal, D.; Sankar, N.; Chandrakaran, S. Effect of reinforcement form on the behaviour of coir geotextile reinforced sand beds. *Soils Found.* **2017**, *57*, 227–236. [CrossRef]
93. Hewlett, W.J.; Randolph, M.F. Analysis of piled embankments. *Ground Eng.* **1988**, *21*, 12–18.
94. King, L.; Bouazza, A.; Dubsky, S.; Rowe, R.K.; Gniel, J.; Bui, H.H. Kinematics of soil arching in piled embankments. *Géotechnique* **2019**, *69*, 941–958. [CrossRef]
95. Han, G.-x.; Gong, Q.-m.; Zhou, S.-h. Soil arching in a piled embankment under dynamic load. *Int. J. Geomech.* **2015**, *15*, 04014094. [CrossRef]
96. Pan, G.; Liu, X.; Yuan, S.; Wang, Y.; Sun, D.; Feng, Y.; Jiang, G. A field study on the arching behavior of a geogrid-reinforced floating pile-supported embankment. *Transp. Geotech.* **2022**, *37*, 100795. [CrossRef]
97. Li, X.; Miao, Y.; Cheng, K. Soil arching effect analysis via a modified finite element model based on a field test. *J. Test. Eval.* **2018**, *46*, 2218–2226. [CrossRef]
98. Meena, N.K.; Nimbalkar, S.; Fatahi, B.; Yang, G. Effects of soil arching on behavior of pile-supported railway embankment: 2D FEM approach. *Comput. Geotech.* **2020**, *123*, 103601. [CrossRef]
99. Meena, N.K. Assessment of Soil Arching in a Pile-supported Railway Embankment under the Moving Train Load and Earthquake. Ph.D. Thesis, University of Technology Sydney, Sydney, Australia, 2022.
100. Oh, Y.I.; Shin, E.C. Reinforcement and Arching Effect of Geogrid-Reinforced and Pile-Supported Embankment on Marine Soft Ground. *Mar. Georesources Geotechnol.* **2007**, *25*, 97–118. [CrossRef]
101. Wang, K.; Cao, J.; Wang, X.; Ning, Y. Soil Arching of Piled Embankment in Equal Settlement Pattern: A Discrete Element Analysis. *Symmetry* **2021**, *13*, 1627. [CrossRef]
102. Kempfert, H.; Göbel, C.; Alexiew, D.; Heitz, C. German recommendations for reinforced embankments on pile-similar elements. In Proceedings of the 3rd European Geosynthetics Conference, Munich, Germany, 1–3 March 2004; pp. 279–284.